Deciphering and modelling the TGF-β signalling interplays specifying the dorsal-ventral axis of the sea urchin embryo

Swann Floc'hlay[1], Maria Dolores Molina[2#], Céline Hernandez[1#], Emmanuel Haillot[2], Morgane Thomas-Chollier[1,3], Thierry Lepage[2]* and Denis Thieffry[1]*,

1. Institut de Biologie de l'ENS (IBENS), École Normale Supérieure, CNRS, INSERM, Université PSL, 75005 Paris, France.

2. Institut Biologie Valrose, Université Côte d'Azur, Nice, France.

3. Institut Universitaire de France (IUF), 75005 Paris, France.

* Corresponding authors
Emails: denis.thieffry@ens.psl.eu ; tlepage@unice.fr
[#] These authors contributed equally to this work.

Abstract

During sea urchin development, secretion of Nodal and BMP2/4 ligands and their antagonists Lefty and Chordin from a ventral organizer region specifies the ventral and dorsal territories. This process relies on a complex interplay between the Nodal and BMP pathways through numerous regulatory circuits. To decipher the interplay between these pathways, we used a combination of treatments with recombinant Nodal and BMP2/4 proteins and a computational modelling approach. We further developed a logical model focusing on cell responses to signalling inputs along the dorsal-ventral axis, which was extended to cover ligand diffusion and enable multicellular simulations. Our model simulations accurately recapitulate gene expression in wild type embryos, accounting for the specification of the three main ectodermal regions, namely ventral ectoderm, ciliary band and dorsal ectoderm. Our model further recapitulates various mutant phenotypes. Temporal analysis revealed the dominance of the BMP pathway over the Nodal pathway, and suggested that the rate of Smad

activation governs D/V patterning of the embryo. These results indicate that a mutual antagonism between the Nodal and BMP2/4 pathways is the fundamental mechanism driving early dorsal-ventral patterning.

Running title: Sea urchin DV axis specification

Key words: *Paracentrotus lividus*, embryo development, logical model, gene regulatory network, Nodal pathway, BMP pathway.

Summary Statement: We propose a predictive computational model of the regulatory network controlling the dorsal-ventral axis specification in sea urchin embryos, and highlight key features of Nodal and BMP antagonism.

Introduction

During embryonic development, cell fate is specified by transcription factors activated in response to instructive signals. Regulatory interactions between signalling molecules and their target genes form networks, called Gene Regulatory Networks (GRN) (Arnone and Davidson, 1997). Deciphering such GRNs is a key for developmental biologists to understand how information encoded in the genome is translated into cell fates, then into tissues and organs, and how morphological form and body plan can emerge from the linear DNA sequence of the chromosomes (Levine and Davidson, 2005). Noteworthy, the gene regulatory network that orchestrates morphogenesis of the ectoderm along the dorsal-ventral axis of the embryo of the model sea urchin *Paracentrotus lividus* has started to be uncovered in great detail (Haillot et al., 2015; Lapraz et al., 2015; Li et al., 2012; Li et al., 2013; Li et al., 2014; Range et al., 2007; Saudemont et al., 2010; Su et al., 2009).

The ectoderm of the sea urchin larva is constituted of two opposite ventral and dorsal territories, separated by a central ciliary band (Fig. 1A):

The ventral ectoderm is the territory at the centre of which the mouth will be formed. Specification of the ventral ectoderm critically relies on signalling by Nodal, a secreted growth factor of the TGF-β family. *nodal* expression is turned on by maternal factors, while Nodal stimulates and maintains its own expression through a positive feedback circuit. Nodal is zygotically expressed and is thought to dimerise with another TGF-β ligand maternally expressed called Univin (Range et al., 2007); the Nodal-Univin heterodimer promotes Alk4/5/7 signalling and the activation of Smad2/3 together with Smad4. The ventral ectoderm boundary is thought to be positioned by the activity of the product of the Nodal target gene *lefty*, which prevents the expansion of *nodal* expression out of the ventral ectoderm region via a diffusion-repression mechanism (Chen et al., 2004; Cheng et al., 2004; Duboc et al., 2008; Sakuma et al., 2002).

The ciliary band ectoderm is a proneural territory located between the ventral and dorsal ectoderm (Angerer et al., 2011). The ciliary band is made of prototypical cuboidal epithelial cells and runs along the arms of the pluteus larva. Unlike specification of the ventral and the dorsal ectoderm, which actively requires TGF-β signalling, specification of the ciliary band

80 tissue does not rely on Nodal or BMP signalling, and this tissue develops as a "default" state
81 of the ectoderm in the absence of these signals.
82
83 The dorsal ectoderm is the territory that will differentiate into the apex of the pluteus larva.
84 Its specification relies on the diffusion of the ventrally synthesized protein BMP2/4, which
85 promotes dorsal fates by activating phosphorylation of Smad1/5/8 via the activation of the
86 BMP type I receptors Alk1/2 and Alk3/6. The inhibition of BMP signalling on the ventral
87 side and the translocation of BMP2/4 to the dorsal side requires the product of the *chordin*
88 gene, which is activated in the ventral ectoderm downstream of Nodal signalling (Lapraz et
89 al., 2009). Glypican5 is expressed downstream of BMP2/4 signalling and contributes to
90 stabilize BMP signalling on the dorsal side by a positive feedback circuit. In addition, the
91 BMP ligands Admp1 and Admp2 provide robustness to signalling fluctuations of BMP
92 through an expansion-repression mechanism and autoregulation (Ben-Zvi et al., 2008; De
93 Robertis, 2009; Joubin and Stern, 2001; Kimelman and Pyati, 2005; Lapraz et al., 2015; Lele
94 et al., 2001; Reversade and De Robertis, 2005; Willot et al., 2002). This mechanism, which
95 relies on the transcriptional repression of *admp1* expression by BMP2/4/ADMP2 signalling,
96 allows *admp1* expression to increase and ADMP1 protein to be shuttled to the dorsal side by
97 Chordin when BMP signalling decreases. Thus, an increase in *admp1* expression
98 compensates for the reduction of the intensity of BMP signalling.
99
100 One prominent feature of the D/V onset specification is that it relies extensively on the
101 maternal inputs Panda and Univin, which respectively represses and promotes ventral fate.
102 Univin is a TGF-β related to Vg1 and GDF1/3 signalling through the Nodal/Activin
103 receptors. Panda is a secreted factor structurally related to members of the TGF-β superfamily
104 presumed to repress ventral fate by a still unidentified mechanism. Finally, the transcriptional
105 repressor Yan/Tel acts as a negative regulator of *nodal* expression, whose function is required
106 downstream of Panda to restrict *nodal* expression to the ventral side (Molina et al., 2018).
107
108 Previous studies have shown that Nodal produced by the ventral ectoderm is a strong
109 ventralising signal. Overexpression of *nodal* causes all ectodermal cells to adopt a ventral fate
110 (Duboc et al., 2004; Lapraz et al., 2015; Saudemont et al., 2010) (Fig. 1B), whereas a loss of
111 Nodal function prevents specification of both ventral and dorsal fates and causes the
112 ectoderm to differentiate as a ciliary band (Fig. 1C). Conversely, the activity of BMP2/4
113 protein promotes dorsalisation, and overexpression of BMP2/4 forces all ectoderm cells to

114 adopt a dorsal fate (Haillot et al., 2015; Lapraz et al., 2009; Lapraz et al., 2015) (Fig. 1D). In
115 contrast, removing the function of the BMP2/4 ligand from fertilization on prevents
116 specification of dorsal fates, leading to formation of an ectopic ciliary band territory in the
117 dorsal region (Fig. 1E). Additionally, knocking down *panda* expression in this BMP2/4 loss-
118 of-function experiment enables *nodal* to be expressed through the dorsal side of the ectoderm
119 and promotes ventral fates in all ectodermal cells (Fig. 1F). Conversely, a local *panda*
120 overexpression specifies the D/V axis by promoting dorsal fates, suggesting that *panda* is
121 sufficient to break the radial symmetry of the embryo and necessary to specify the D/V axis.
122 The BMP and Nodal ligands thus show strongly antagonistic activities. However, the
123 mechanism underlying this antagonism and the resulting cell fate decision still awaits
124 clarification.
125
126 Due to the largely non-cell autonomous nature of the D/V GRN and to the many events of
127 protein diffusion and feedback circuits involved, an intuitive understanding of the logic of the
128 network is hard to obtain. For example, Nodal and BMP2/4 are co-expressed in the ventral
129 territory, but active signalling pathways are located at opposite poles of the D/V axis. In this
130 context, a model of the D/V gene regulatory network is very useful to formalize the complex
131 regulatory interactions at stake (Wilczynski and Furlong, 2010). A Gene Regulatory Network
132 can be modelled as a static regulatory graph with standardized annotations to represent
133 molecular interactions between key regulator components (Arnone and Davidson, 1997). This
134 regulatory graph can be supplemented with threshold levels and regulatory rules to obtain a
135 predictive, dynamical model (Mbodj et al., 2016; Peter, 2019; Peter et al., 2012; Thomas and
136 D'Ari, 1990).
137
138 In the present study, we built a logical model (i.e. using Boolean algebra for the regulatory
139 rules) of the sea urchin dorsal-ventral specification GRN to (i) assess its accuracy, (ii)
140 compare the model predictions for different perturbations with the observed gene expression
141 patterns, (iii) explore the dynamics of the system, and (iv) develop a multicellular framework
142 to test the ability of the model to generate the spatial patterns observed in wild type or
143 perturbed embryos.
144

Results

Model building

We constructed a model of the GRN driving the D/V patterning of the sea urchin ectoderm. We started by compiling experimental data to identify the key genes and regulatory interactions (Fig. 2). The raw data that provided the spatial and temporal expression information to build the model were derived from high resolution in situ hybridization analysis, Northern blot experiments and systematic perturbations experiments. Loss-of-function experiments via morpholino injections are particularly important for GRN reconstruction since they allow to test if a gene is required for activation of another gene. Gain-of-function experiments via mRNA injection were also used in many instances to test for the ability of a given gene to induce another gene when overexpressed.

Based on these data, we first built a regulatory graph representing the D/V GRN in a single cell, using the software GINsim (ginsim.org) (Chaouiya et al., 2012). This construction is an iterative process: the model is subjected to simulations that are confronted to experimental data, and the network and regulatory rules are progressively refined until the simulations qualitatively recapitulate the experimental observations (Fig. 2).

We present here the final model and the simulations (cf. section below) that recapitulate the patterns observed experimentally. The model encompasses a total of 31 nodes, linked by 25 activations and 16 inhibitions (Fig. 3). The nodes included into the model correspond to signalling and regulatory components, while the signed arcs denote regulatory effects between these components. Signalling factors are modelled as input nodes (in yellow in Fig. 3), providing activating or inhibiting signals through the corresponding membrane receptors.

Each non-input node is classified as ventral (eleven nodes shown in blue in Fig. 3), ciliary band (two nodes shown in pink in Fig. 3) or dorsal (eight nodes shown in green in Fig. 3), according to the reported location and time of activation in the presumptive ectodermal regions. For example, *goosecoid* is activated by the Nodal cascade in the ventral region in wild-type condition, and is thus considered as a ventral gene. The model encompasses the main regulatory components of TGF-β signalling pathways, including the ligands, negative regulators such as the proteins that trigger receptor degradation, downstream transcription factors, and antagonists. Each node of the model is annotated with textual explanations and

179 database links (in particular to PubMed) documenting our modelling assumptions (main
180 references include the GRN diagram published for Paracentrotus lividus in (Haillot et al.,
181 2015; Lapraz et al., 2006; Lapraz et al., 2015; Range et al., 2007; Saudemont et al., 2010)).
182
183 Among the 31 components of the model, 22 are associated with Boolean variables (ellipsoid
184 nodes in Fig. 3, taking the values 0 or 1 depending on their activation state), while the
185 remaining components are associated with multilevel variables (rectangular nodes in Fig. 3,
186 associated with three or four integer levels, from zero to 2 or 3, see below). The nine input
187 nodes (shown in yellow in Fig. 3) define 2,304 possible input value configurations. Using the
188 Java library bioLQM (Naldi, 2018), we identified 1,258 stable states, which can be split into
189 three main patterns based on the active nodes: 456 ventral, 450 ciliary and 352 dorsal patterns
190 (cf. Jupyter notebook).
191
192 <u>An antagonism between the Nodal and BMP2/4 pathways drives allocation of cell fates along</u>
193 <u>the dorsal-ventral axis.</u>
194 A key feature of the D/V GRN is the strong antagonistic activities of BMP2/4 and Nodal. To
195 correctly account for this aspect in the model, additional experiments were conducted to
196 better characterize the underlying mechanisms. We first tested whether difference in relative
197 intensity between both pathways could favour the establishment of one cell fate over the
198 other. Treatment with an intermediate dose of BMP2/4 protein resulted in embryos
199 developing with a straight archenteron, no mouth, and covered with a ciliary band like
200 ectoderm (Fig. 4A), which is a prototypical Nodal loss-of-function phenotype. Similarly, at
201 intermediate doses of Nodal, the embryos developed with a reduced apex, a phenotype
202 resembling the BMP2/4 loss-of-function phenotype. These observations suggest that
203 ectodermal cells receive both antagonistic ventralising Nodal and dorsalising BMP2/4
204 signals, and integrate them even at intermediary doses at the level of the *cis*-regulatory
205 sequences of their target genes.
206
207 However, since these treatments were performed soon after fertilisation, it was not clear
208 whether the outcome was reflecting an antagonism between Nodal and BMP occurring during
209 cell fates allocation, or if they were only the consequence of one pathway being activated
210 early and dominantly in all cells of the embryo following the injection of mRNA into the egg.
211 To address this issue, we repeated the Nodal and BMP2/4 treatment at late blastula or early
212 mesenchyme blastula stage. Treatments with Nodal or with BMP2/4 proteins at late blastula

213 radialised the embryos by respectively inducing ventral or dorsal fate in all ectodermal cells
214 (Fig. 4B). These results confirm that the Nodal and BMP2/4 pathway act antagonistically also
215 during the fate specification phase and that a competition based on dosage rather than on time
216 of activation is driving the regulation. In order to take into account these results , we paid a
217 particular attention to the encoding of this antagonism in our model.
218 First, we associated nine nodes of the model with ternary or quaternary variables (rectangular
219 nodes in Fig. 3, taking values from 0 to 2 or from 0 to 3, respectively). These multivalued
220 nodes allow for a more fine-grained encoding of the activation states of key morphogens and
221 downstream components whose effects are dose-sensitive (nodes Nodal_In, Chordin_In,
222 BMP2_4_In, Alk4_5_7, Alk2_3_6, Smad2_3_4, Smad1_4_5_8 in Fig. 3). Second, the
223 antagonism between the Nodal and BMP pathways is encoded in the model in the form of a
224 double reciprocal inhibition between Smad2_3_4 and Smad1_5_8_4 (Fig. 3), which
225 implements the competition of these signalling complexes for the shared molecule Smad4.
226 Note that each of these two inhibitory interactions can be counteracted by an increased
227 activity of the other antagonistic pathway, following the dose-dependent competition
228 hypothesis (this is encoded in the corresponding logical rules, see Table 1).
229
230 <u>Model stable states match experimental wild-type and morphants phenotypes.</u>
231 To test our model, we ran simulations and compared the resulting stable states with the wild
232 type phenotypes observed experimentally. We applied different sets of values for the inputs
233 nodes, each set corresponding to a specific territory of the ectoderm (Table 1 and Materials
234 and methods). Using proper combinations of active inputs, the model returns stable state(s),
235 which are then compared with the list of marker genes expected to be expressed in the
236 corresponding territory, based on *in-situ* hybridization experiments. We first ran simulations
237 using initial states corresponding to early 32-cell stage embryos signalling (Fig. 5A),
238 preceding the later blastula stage. This stage corresponds to the onset of specification of the
239 ventral organiser, which forms at the opposite side of the gradient of Panda mRNA (Haillot et
240 al., 2015). This pattern is correctly recapitulated by the stable states obtained from the wild-
241 type simulations (Fig. 5B-C). The resulting stable states were then used to specify the initial
242 conditions reflecting a later blastula stage of embryogenesis, after diffusion and shuttling of
243 maternal factors have taken place (Fig. 5B). Indeed, as multiple diffusion events occur, some
244 model inputs expressed in one territory are active in a broader region for blastula simulations
245 (Fig. 6A).

246 After some iterative refinements of the rules, model simulations qualitatively recapitulated
247 the expression patterns expected for each individual territory (ventral, ciliary, dorsal) (Fig.
248 6B). Hence, we can conclude that, the regulatory graph shown in Fig. 3 supplemented by the
249 logical rules of Table 1 are sufficient to specify the three main ectodermal D/V patterns of the
250 sea urchin embryo.
251
252 To further validate and explore the properties of our model, we simulated loss- or gain-of-
253 function experiments (mRNA or morpholino injection) by restricting the range of reachable
254 levels for one or multiple node(s), e.g. to zero for a loss-of-function, or to a higher value for a
255 gain-of-function (cf. Material and methods). As in the wild-type conditions, we assessed the
256 relevance of our model by comparing the resulting stable states with the patterns observed in
257 the corresponding *in-situ* experiments following mRNA or Morpholino injection in the
258 embryo at early stage. For seven of the eight mutants simulated, the model returned a unique
259 single stable state in each region, which qualitatively matched experimental observations
260 (Fig. 6B-D).
261
262 In the cases of *nodal* Morphants and of *lefty* mRNA overexpression, the ventral cascade fails
263 to be established, leading to the absence of both Nodal and BMP2/4 pathways, and the
264 presence of a default ciliary state in all the ectodermal cells. Following *nodal* mRNA
265 overexpression, competition between Smad2/3 and Smad1/5/8 for Smad4 creates an
266 advantage for the ventral cascade producing a fully ventralised embryo. The same pattern is
267 obtained for the *lefty* Morpholino, because this perturbation impacts the diffusion-repression
268 mechanism controlled by Lefty (Juan and Hamada, 2001), enabling *nodal* expression to
269 propagate without restriction (Duboc et al., 2008). In the case of overexpression of the dorsal
270 fate repressor *chordin* or in the case of BMP morphants, the absence of BMP2/4 signalling
271 fosters a ciliary band state in the presumptive dorsal territory. However, as BMP2/4 is not
272 necessary for the expression of *nodal*, the ventral cascade maintains a wild-type expression
273 pattern in these morphants. Finally, following *bmp2/4* overexpression, the competition for the
274 common Smad is driven toward the activation of the dorsal cascade, giving a fully dorsalised
275 ectoderm state.
276
277 Interestingly, in the case of the *chordin* morpholino, the model returned two stable states
278 (denoted by the green and blue triangles at the bottom of Fig. 6B) in the presumptive ventral

279 region, corresponding to ventral and dorsal fates, respectively. This situation is hereafter
280 further investigated using a probabilistic framework.
281
282 Stochastic logical simulation of the *chordin* Morphants
283 Using stochastic simulations, one can unfold the temporal dynamics of the regulatory
284 network for given initial conditions and estimate the prevalence of any reachable stable state.
285 In the case of the ventral region in *chordin* morphant conditions, we have seen that our model
286 can reach two different stable states, corresponding to ventral and dorsal expression patterns.
287 Using the software MaBoss (https://maboss.curie.fr) (Stoll et al., 2017), we performed
288 stochastic temporal simulations of our model to generate mean time plots and estimate the
289 probability to reach each of these stable states. In the absence of precise kinetic information,
290 we first used equal rates for all (up or down) state transitions.
291 In the wild type ventral region, as expected, all stochastic simulations gave rise to a ventral
292 expression pattern (Fig. 7A). In contrast, for the *chordin* morphant, the dorsal state is reached
293 about twice as often as the ventral state (Fig. 7B). In other words, the dorsal pathway is more
294 likely to win the competition for Smad4. This partial dominance of the dorsal pathway
295 matches the experimental observations of weak dorsal patterns for *chordin* morphants (Fig.
296 6D), presumably resulting from the co-activation of the two antagonistic pathways.
297
298 In the *chordin* morphants, BMP signalling goes unrestricted in the ventral ectoderm,
299 promoting dorsal fates and repressing the ventral cascade. However, since Nodal is critically
300 required for *bmp2/4* activation, *nodal* down-regulation in turn leads to the repression of
301 BMP2/4 signalling. Therefore, in the absence of Chordin, both the ventral and dorsal
302 cascades are activated through feedback circuits. This conclusion is supported by
303 experimental observation of transient Smad1/5/8 signalling and *tbx2/3* expression in the
304 ventral ectoderm (Lapraz et al., 2009).
305
306 To further assess whether this imbalance in favour of the dorsal pathway activation is
307 sensitive to kinetic (transition) rates, we ran stochastic simulations with different Smad
308 activation rates for the two pathways. An imbalance in favour of the dorsal Smad activation
309 increased the gap between the final proportion of dorsal and ventral stable state compared to
310 wild type (Fig. 7C). On the contrary, an imbalance in favour of the ventral Smad activation
311 inversed the relationship, with a higher fraction of ventrally specified states than dorsally

312 specified states, almost mirroring the ratios obtained with equiprobable transition rates (Fig.
313 7D).
314
315 In conclusion, the outcome of the competition between the two pathways is strongly sensitive
316 to the kinetic rates for the activation of the different Smads. The pathway specific Smad
317 firstly activated immediately represses the other one by pre-empting Smad4 and thereby
318 fosters the corresponding state stable.
319
320 Multicellular simulations emphasize the crucial role of long-range signal diffusion
321 In the preceding section, we simulated the behaviour of cells of the three different
322 presumptive territories by selecting appropriate combinations of signalling input levels,
323 which were considered as fixed for the whole duration of the simulations. To model more
324 precisely the production and diffusion of signalling molecules across the ectoderm, we used
325 the software EpiLog (https://epilog-tool.org) (Varela et al., 2019), which supports simulations
326 of an epithelium encompassing multiple cells connected through signalling of diffusing
327 elements. The behaviour of each cell of the epithelium is modelled by the same cellular
328 logical model, but levels of input signal directly depend on the signal values output by
329 neighbouring cells. The input signals perceived by a given cell are integrated into logical
330 diffusion rules, and updated synchronously (see Materials and methods and Table 2) (Fig.
331 8A). Hence, in general, input levels change over time.
332
333 To simulate the wild type condition, we initialised the model with a small concentration of
334 Nodal and Smad2/3/4 in the ventral territory (corresponding to the three left-most range of
335 cells) (Fig. 8B). This simulation correctly recapitulated the expected contiguous ventral,
336 ciliary and dorsal ectoderm territories (Fig. 8C). This result suggests that the relatively simple
337 diffusion rules properly account for the dynamics of the proteins governing the dorsal-ventral
338 patterning. In addition, this result highlights the crucial role of Nodal to direct specification of
339 the ectoderm along the whole dorsal-ventral axis.
340 As in the case of the unicellular model, we can apply specific perturbations to assess their
341 impact at the tissue level. As shown in Fig. 8C, our multicellular simulations accurately
342 recapitulated the phenotypes of the different morphant patterns observed experimentally.
343 Note that the chordin morpholino has been discarded from these simulations, as it gave rise to
344 two different stable states, which cannot be covered with the Epilog deterministic input
345 updating approach. Interestingly, in the course of *lefty* morpholino simulation, we could

346 clearly see a shift in the ventral-ciliary frontier, which progressively moved toward the dorsal
347 side, as Nodal diffused in the absence of Lefty repression, until it reached the fully
348 ventralised stable state (see Fig. S1).
349
350 Using Epilog, it is further possible to perform local perturbations by modifying the initial
351 levels of one or several signalling molecules at specific epithelium locations. Using this
352 feature, we could recapitulate in silico the results of an experiment reported by (Lapraz et al.,
353 2015), who injected *nodal* mRNA into two opposite cells of a 4-cell stage *nodal* knock-down
354 embryo (i.e. following a *nodal* Morpholino injection in the egg). This experiment triggered
355 the formation of an ectopic, inverted D/V axis and resulted in the development of siamese
356 pluteus larvae with two ventral sides, two ciliary bands and a central dorsal territory. Using
357 Epilog and imposing *nodal* and *smad2/3/4* activity at the initial state in both the ventral and
358 the dorsal side of the epithelium, our spatial logical simulation qualitatively reproduced the
359 siamese pattern observed experimentally (Fig. 8D).
360

361 **Discussion**

362

363 Gene regulatory networks integrate documented interactions between transcription factors,
364 signalling components, and their target genes, which ultimately translate the information
365 encoded into the genome into morphological form and body plan. However, as our
366 delineation of developmental systems progresses, we are facing increasingly large and
367 complex networks, which cannot be fully and rigorously understood without proper
368 formalisation. This is, for example, clearly the case for the GRN governing D/V patterning of
369 the sea urchin embryo, which relies on numerous signalling and regulatory factors, involved
370 in multiple positive and negative feedback circuits.

371

372 In our modelling study, several key choices had to be made. As little is known regarding
373 detailed mechanisms and kinetic parameters, we opted for a qualitative, logical formalism.
374 However, to properly model morphogen diffusion and dose-dependent effects, we considered
375 a multilevel extension of the classical Boolean framework. Importantly, in the course of its
376 conception, the model was systematically tested through extensive simulations of wild-type
377 and perturbed conditions. In wild-type conditions, our unicellular model fully recapitulated
378 each territory pattern independently. We further took advantage of a recent multicellular
379 extension of the logical framework to explicitly simulate spatial pattern formation, whose
380 results can be more easily compared directly with the phenotypes of wild-type and mutant
381 embryos.

382

383 A key step in our study was to model the interplay between the Nodal and BMP pathways. In
384 this respect, we were guided by our experiments dealing with the treatment of embryos with
385 recombinant Nodal or BMP2/4 proteins at blastula stage (i.e. after the initial specification of
386 the ventral and dorsal territories). These experiments, which demonstrated that over-
387 activation of one of these pathways is sufficient to abrogate signalling from the other
388 pathway, highlighted the strong antagonism between Nodal and BMP2/4 signalling and
389 suggested that this antagonism resulted from a direct competition between the two pathways
390 activated by these TGF-βs ligands rather than from their timing of activation.

391

392 The competition between Nodal and BMP2/4 played a key role in understanding the
393 regulatory dynamics within the *chordin* knock-down experiments, which was the only
394 morphant not fully recapitulated by our model for all three territories. In the case of the

395 *chordin* knock-down, our logical model predicted that both the ventral and dorsal steady
396 states were possible in the presumptive ventral region. Accordingly, in the *chordin* morphant,
397 both the Nodal and the BMP2/4 pathways are activated, antagonising each other.
398 Consequently to this ectopic activation of BMP signalling, the ventral territory in *chordin*
399 morphants displays a transient dorsalisation, before reversing towards a ventral ectoderm fate
400 during gastrulation, as shown by the presence of a mouth opening. However, this brief
401 dominance of the dorsal fate over the ventral fate in the conditions of Nodal and BMP2/4 co-
402 activation is not well understood. To further explore the underlying regulatory mechanism of
403 this dorsal fate dominance, we performed a stochastic logical simulation of the unicellular
404 model in *chordin* knock-down condition. This analysis resulted in a higher proportion of
405 active dorsal fates over ventral fates, in agreement with the experiments. This result suggests
406 that the transient dorsal dominance is encoded in the structure of the GRN. Indeed, even in
407 the case of the *chordin* morphants, the model accurately recapitulates the conflict caused by
408 the coactivation of the Nodal and BMP2/4 pathways in the ventral ectoderm. However, by
409 modulating the rates associated with the different Smads and performing additional
410 simulation, we showed that the outcome of the competition between the two pathways is
411 strongly sensitive to these rates.
412
413 At this point, our model remains limited to the major early dorsal-ventral patterning events
414 occurring in the sea urchin embryo. However, in the future, this model could be tentatively
415 extended to integrate novel data and to explore more refined specification and differentiation
416 events. For example, it could be extended to investigate the specification of the boundary
417 ectoderm region, located at the interface between the ectoderm and endomesoderm, which
418 plays a central role in positioning the clusters of primary mesenchyme cells and spicules
419 patterning (Armstrong and McClay, 1994; Armstrong et al., 1993; Duloquin et al., 2007;
420 Hardin et al., 1992; Röttinger et al., 2008). This process is known to depend on Wnt
421 signalling, presumably in conjunction with Nodal, BMP2/4 and ADMP2 signalling (Lapraz et
422 al., 2015; McIntyre et al., 2013; Röttinger et al., 2008; Saudemont et al., 2010). With the
423 current unicellular model, the simulation with the input levels corresponding to the boundary
424 ectoderm (i.e. Admp2 and Wnt active) results in a dorsal stable state (Fig. S2).
425
426 Another possible addition to the model would be the integration of the negative feedback of
427 Smad6 on BMP2/4 pathway (Armstrong and McClay, 1994; Armstrong et al., 1993;
428 Duloquin et al., 2007; Hardin et al., 1992; Röttinger et al., 2008). Indeed, Smad6 is activated

429 by the dorsal signalling downstream of BMP2/4 ; it buffers the activation of the dorsal
430 pathway by acting as an inhibitor on BMP2/4 signalling. Such a negative feedback circuit
431 typically generates an oscillatory behaviour. In the frame of the Boolean logic, the
432 consideration of this negative feedback circuit would result in a cyclic attractor with
433 alternation of active and inactive BMP and Smad6 activities, which are more difficult to
434 interpret than stable states.
435
436 Our logical model focuses on the blastula and gastrula developmental stages of sea urchin
437 embryogenesis. One possible extension would be to further explore the regulatory
438 interactions taking place at earlier stages. In the case of the 32-cell stage, our model correctly
439 recapitulates wild-type pattern mainly driven by Panda expression. Furthermore, the
440 simulation results of Panda loss-of-function in 32-cell stage conditions mirror the fully
441 ventralised phenotype obtained experimentally (Haillot et al., 2015) (Fig. S3 A-B). However,
442 the simulations of Panda overexpression show discrepancies relative to the experimental
443 observations. In this case, our model predicts the ventral region become dorsalized, whereas
444 global injection of *panda* mRNA does not impact the wild-type pattern. Indeed, current
445 models suppose that an asymmetry of *panda* mRNA provides the spatial cue that in turn
446 controls the polarised activation of downstream genes. Therefore, an asymmetry of *panda*
447 mRNA or of Panda protein constitutes the main driving signal to allocate cell fates, rather
448 than a change in overall Panda concentration. This signalling based on multicellular gradient
449 cannot be currently recapitulated by our unicellular model, as it requires to integrate inputs
450 from multiple surrounding cells and also to rely on relative differences in concentration
451 instead of absolute levels. Further development of EpiLog features could enable us to build
452 logical rules accounting for the specificities of such multicellular gradient signalling.
453
454 To conclude, we have shown that logical modelling can capture several salient dynamical
455 features of the GRN governing early dorsal-ventral patterning of sea urchin embryos,
456 including the key role played by intercellular interactions. Such models should therefore be
457 useful to further explore the complex interplay between maternal factors and zygotic genes,
458 which orchestrates patterning of the ectoderm of the sea urchin embryo downstream of
459 intercellular signals. To this end, we provide our models and the Jupyter notebook
460 implementing all our analyses within the CoLoMoTo docker environment (see supplementary
461 materials).
462

463 **Materials and methods**

464

465 Animals, embryos and treatments

466 Adult sea urchins (*Paracentrotus lividus*) were collected in the bay of Villefranche-sur-Mer.
467 Embryos were cultured as described in (Lepage and Gache, 1989; Lepage and Gache, 1990).
468 Fertilization envelopes were removed by adding 1mM 3-amino-1,2,4 triazole (ATA) 1 min
469 before insemination to prevent hardening of this envelope followed by filtration through a 75
470 µm nylon net. Treatments with recombinant BMP2/4 or Nodal (R&D) proteins were
471 performed at the time indicated in the schemes by adding the recombinant protein diluted
472 from stocks in 1 mM HCl in 24 well plates containing about 1000 embryos in 2 ml of
473 artificial sea water (Lapraz et al., 2009).

474

475 Anti-phospho-Smad1/5/8 Immunostaining

476 Embryos were fixed with 4% formaldehyde for 15 min at swimming blastula stage (3 hours
477 after adding BMP2/4 protein) then briefly permeabilized with methanol. Anti-Phospho-
478 Smad1 (Ser463/465) / Smad5 (Ser463/465) / Smad9 (Ser465/467) from Cell Signalling
479 (D5B10 Ref. 13820) was used at 1/400. Embryos were imaged with an Axio Imager.M2
480 microscope.

481

482 *In situ* hybridization

483 *In situ* hybridization was performed using standard methods (Harland, 1991) with DIG-
484 labelled RNA probes and developed with NBT/BCIP reagent. The *nodal*, *chordin* and *tbx2/3*
485 probes have been described previously (Duboc et al., 2004; Lapraz et al., 2009). Control and
486 experimental embryos were developed for the same time in the same experiments. Embryos
487 were imaged with an Axio Imager M2 microscope.

488

489 Overexpression of mRNAs and morpholino injections

490 For overexpression studies, *nodal, lefty, chordin* and *bmp2/4* capped mRNAs were
491 synthesized from NotI-linearized templates using mMessage mMachine kit (Ambion). After
492 synthesis, capped RNAs were purified on Sephadex G50 columns and quantitated by
493 spectrophotometry. *Nodal , lefty*, *chordin* and *bmp2/4* mRNAs were injected at 400 µg/ml,
494 200 µg/ml, 1000 µg/ml and 500 µg/ml, respectively. Capped mRNA were injected mixed
495 with Tetramethylrhodamine Dextran (10000 MW) at 5 mg/ml (Duboc et al., 2004).
496 Morpholino oligonucleotides were dissolved in sterile water and injected at the one-cell stage

497 together with Tetramethylrhodamine Dextran (10000 MW) at 5 mg/ml as already described
498 (Duboc et al., 2004; Haillot et al., 2015).
499
500 Logical formalism
501 We built our model using the multilevel logical formalism introduced by R. Thomas (Thomas
502 and D'Ari, 1990). This qualitative approach relies on graph-based representations of the
503 network and of its dynamics. The network is formalized as a *regulatory graph*, where nodes
504 denote molecular species (e.g. proteins), whereas signed arcs denote regulatory interactions,
505 positive or negative. The nodes can take a limited number of integer values, only two (0 or 1)
506 in the simplest, Boolean case, but potentially more when biologically justified, for example in
507 the case of morphogens with clearly distinct activity ranges. Hence, each regulatory arc is
508 associated with an integer threshold, always 1 in the Boolean case, but potentially higher in
509 the case of a multilevel regulator. Logical rules further specify how each node reacts to the
510 presence or absence of the corresponding incoming interactions. Specific (non-overlapping)
511 Boolean rules are defined for each value of each node.
512 Boolean rules are built by combining literals (i.e. valued component) with the logic operators
513 AND (denoted "&"), OR (denoted "|") and NOT (denoted "!").
514 Table 1 lists the formula associated with the different components of our model.
515 Note that the formula associated with zero values are omitted, as they can be computed
516 directly as the complement of the formulae defined for the other values for a given node.
517 For example, the formula of the node FoxA
518 FoxA => 1 IFF (FoxA | Brachyury) & !Repressor_R1"
519 can be translated into "FoxA node tends toward the value 1 if and only if FoxA or Brachyury
520 are active and Repressor_R1 is not active".
521 In this example, the regulatory actions from Brachyury to FoxA and from Repressor_R1 to
522 FoxA correspond respectively to an activation and an inhibition.
523 The levels of the input (unregulated) nodes are defined at the start of simulations.
524 Using the Boolean rules of Table 1, we can simulate the behaviour of the system for different
525 input value combinations. In this respect, we use the asynchronous updating approach
526 proposed by R. Thomas (Thomas, 1991), which consists in following all the different
527 possible single unitary changes of values induced by the rules.
528 The dynamical behaviour of the model is generally represented in terms of a *state transition*
529 *graph*, where each node represents a discrete state of the model (i.e. a vector listing the

530 values of the different components of the model), whereas each arc represents a state
531 transition.
532 In this work, we took advantage of the implementation of this logical formalism into the user-
533 friendly Java software suite GINsim (version 3.0, see http://ginsim.org, (Naldi, 2018)). In our
534 analyses, we particularly focused on stable states (see e.g. Fig. 5B), which typically denote
535 cell differentiation states. These can be directly computed (i.e. without unfolding the state
536 transition graph) using a very efficient algorithm implemented in GINsim (Naldi et al., 2007).
537
538 Wild type simulation
539 We simulated the behaviour of each dorsal-ventral region independently, considering
540 different sets of values for the input nodes in the ventral, ciliary and dorsal presumptive
541 territories. These sets of input values were defined based on previously published results (see
542 Results section). As we simulate each territory individually, the unicellular model cannot
543 directly take into account the diffusion of morphogens, which are therefore specified as input
544 levels (e.g. the presence of Lefty is considered as an active input in the ciliary regions,
545 although it is known that it diffuses from the ventral region). For each simulation, we extract
546 the resulting stable state(s) and classify them as ventral, ciliary or dorsal pattern depending on
547 the set of output node levels.
548 For example, the initial conditions for the simulation of the ventral ectoderm territory
549 considered as active inputs Nodal (level 2), Lefty, Chordin and BMP2/4. This combination
550 produced a stable state in which all the ventral nodes were active and the dorsal nodes
551 inactive. In contrast, when the initial conditions were set as Nodal (level 1), Lefty. BMP2/4,
552 Chordin and Tolloid being active, the resulting stable state corresponded to the dorsal
553 regulatory state.
554
555 Mutant simulations
556 Genetic perturbations are defined in GINsim by constraining one or sometimes several nodes
557 of the model. To simulate a *knock down* mutant (e.g. injection of a morpholino), the level of
558 the corresponding node is set and maintained to 0. In the case of an ectopic expression (e.g.
559 injection of a mRNA), the level of the corresponding node is set and maintained to its
560 maximal value, which can be 1 or higher in case of a multilevel node. Morphogen diffusion is
561 taken into account through the specifications of proper input values, which thus need to be
562 adjusted for each mutant. For example, the ectopic activation of Nodal is known to induce the

activation of its downstream target BMP2/4 very early on; hence, the corresponding input variables must be set at their highest levels for the simulation of ectopic nodal expression.

Stochastic modelling using MaBoss

When several stable states can be reached (as in the case of *chordin* morpholino), we have performed probabilistic simulations to evaluate the probability to reach each of these stable states from the specified initial conditions. In this respect we used the software MaBoss (https://maboss.curie.fr), a C++ software enabling the simulation of continuous/discrete time Markov processes, applied to Boolean networks. The original unicellular model is converted into the MaBoSS compliant format using a specific export functionality of GINsim, which involves the replacement of multilevel nodes by sets of Boolean variables, without affecting the model dynamic (Stoll et al., 2017). Per default, all up and down rates are considered equal, but these can be modified at will.

In this study, we used MaBoSS to simulate the *chordin* morpholino perturbation (comparing it with the wild-type situation), which resulted in two possible stable states in the unicellular model. The inputs were fixed as for the ventral configuration (Nodal, Lefty, BMP2/4 and Admp1 active) in the presence or inactivation of Chordin. We then modified the propensity to activate the ventral or the dorsal cascade by adjusting the ratios of the rates assigned to the Alk receptors corresponding to each of the two cascades: 0.5/0.5 (equiprobable rates), 0.75/0.25 (ratio favouring the dorsal Alk), 0.25/0.75 (ratio favouring the ventral Alk).

Multicellular simulation using EpiLog

We took advantage of recent software Epilog (https://epilog-tool.org, v1.1.1.) (Varela et al., 2019) to perform multicellular simulations. The use of Epilog implies the definition of additional logical rules for the diffusion of signals, e.g. of the values of input nodes depending on the output nodes active in neighbouring cells, taking into account their distance from the target cell. For example, the rule "{Nodal:2[0:1], min = 3}" states that a cell will have its Nodal input node value converging toward the value 2 if at least 3 cells are expressing Nodal at a value 2 at a maximum distance of one cell (i.e. the target cell itself and its direct neighbours).

Our epithelium model is eight cells wide and six cells long, made of hexagonal shaped cells, each one being in direct contact with at most six different neighbouring cells. The top and bottom part of the epithelium are wrapped together to allow diffusion of signalling molecules through these two sides. Each cell behaves according to the model described in our

unicellular simulations. In contrast with our previous unicellular simulations, the inputs are dynamically updated based on the signals perceived in each cell, depending on the activation levels of the output nodes of neighbouring cells. The rules integrating the extracellular signals are identical for all cells of the epithelium. In our epithelium simulations, input nodes of all cells are updated in a synchronous manner. Hence, each epithelium simulation gives rise to a deterministic trajectory ending in a single attractor at the level of the whole tissue (a stable state for the simulations reported here).

Multicellular wild type and mutant simulations

For our epithelium simulations, we define the initial state by selecting the nodes that will be active in a specific set of cells at the start of the simulation. During simulations, the values of these nodes can change depending on the model state and on paracrine signalling. To simulate a wild-type embryo, we set the model to an initial state where the ventral cascade is starting to be activated in the ventral region of the epithelium (3 leftmost cell columns of the epithelium), with the initial and transient activation of Smad1_4_5_8 and Nodal output nodes. Univin is also ubiquitously present at initial state. As in the unicellular simulation, for simulating perturbations, the target nodes are set and maintained at a fixed value.

For the siamese simulation, we use the wild-type logical model with a larger epithelium, with an initial state accounting for a ventral expression of Smad1_4_5_8 and Nodal on the ventral side, but also on the dorsal side of the epithelium (3 rightmost cell columns of the epithelium), i.e. a symmetrical activity pattern.

Model and code availability

The unicellular and multicellular models, together with the Jupyter notebook encoding all the simulations performed with GINsim and MaBoss, are available in the GINsim model repository (http://ginsim.org/node/236) and the GitHub repository https://github.com/ComputationalSystemsBiology/echinodal_notebook. The Jupyter notebook uses the colomoto-docker image (https://github.com/colomoto/colomoto-docker, v2020-01-24) (Naldi et al., 2018). The models can be uploaded in zginml and peps format, to be open with GINsim (v3.0.0b) and EpiLog (v1.1.1), respectively. The unicellular model has been further deposited in SBML qual format in the BioModels database (ID MODEL2002190001).

Table 1

A - Input nodes	Value ventral	Value ciliary	Value dorsal
Nodal_In	2	1	1
Lefty_In	1	1	1
Panda_In	0	0	0
Admp1_In	1	1	1
Bmp2_4_In	1	1	1
Chordin_In	1	1	1
Tolloid_In	0	0	1
Wnt_In	0	0	0
Admp2_In	0	0	0

B - Internal nodes	Value	Logical rule	Expression	Initial state
Univin	1	!Smad2_3_4:2	Ventral	1 (basal)
Alk4_5_7	1	(Nodal_In:1 & !Lefty_In & Univin & !Panda) | (Nodal_In:2 & Univin & !Panda)	Ventral	0
Alk4_5_7	2	Nodal_In:3 & Univin	Ventral	0
Smad_2_3_4	1	Alk4_5_7:1 & !Smad1_4_5_8 & !Smad6	Ventral	0
Smad_2_3_4	2	Alk4_5_7:2	Ventral	0
Nodal	2	Smad2_3_4	Ventral	0
Bmp2_4	1	Smad2_3_4:1	Ventral	0
Bmp2_4	2	Smad2_3_4:2	Ventral	0
Lefty	1	Smad2_3_4	Ventral	0
Chordin	1	Smad2_3_4	Ventral	0
Goosecoid	1	Smad2_3_4	Ventral	0
Repressor_R1	1	!Goosecoid	Ventral	0
FoxA	1	(FoxA | Brachyury) & !Repressor_R1	Ventral	0
Brachyury	1	!Repressor_R1 | FoxA	Ventral	0
Alk1_2_3_6	1	((Admp2_Trans & !Chordin_In) | (Admp2_Trans & Tolloid_In & !Chordin_In:2)) & !Bmp2_4_In:2	Dorsal	0
Alk1_2_3_6	1	((Bmp2_4_In:1 & Admp1_In & !Chordin_In) | (Bmp2_4_In:1 & Admp1_In & Tolloid_In & !Chordin_In:2)) & !Bmp2_4_In:2	Dorsal	0
Alk1_2_3_6	2	Bmp2_4_In:2 & !Chordin_In:2	Dorsal	0
Smad1_4_5_8	1	Alk1_2_3_6:2 & Smad2_3_4:2	Dorsal	0
Smad1_4_5_8	2	(Alk1_2_3_6:2 & !Smad2_3_4:2) | (Alk1_2_3_6:1 & !Smad2_3_4)	Dorsal	0
Tbx2_3	1	Smad1_4_5_8:2	Dorsal	0
IrxA	1	Tbx2_3	Dorsal	0
Smad6	1	Tbx2_3 | Smad1_4_5_8:2	Dorsal	0
Glypican5	1	Smad1_4_5_8:2	Dorsal	0
Frz	1	Wnt_In	Dorsal	0
Admp2	1	Frz | Smad1_4_5_8:2	Dorsal	0
FGFA	1	!Smad2_3_4 & !Smad1_4_5_8:2	Ciliary	0
Onecut	1	!(IrxA | Goosecoid | Smad2_3_4)	Ciliary	0

632 **Table 1. Logical rules of the unicellular model.**

633 Logical rules are used to define the behaviour of each node, for each territory, relative to its
634 direct upstream regulatory nodes. Input nodes (A) do not have any assigned rule, as they are
635 set to a given fixed value specific for each territory when performing simulations. Internal
636 nodes (B) have a logical rule assigned for each possible level they can converge to and an
637 initial state. All nodes have a basal level of 0 (inactive), except Univin (basal level 1), as it
638 tends to be ubiquitously active without the need for activators. The logical rules combines
639 literals, each representing the activity of one node, with the Boolean operators OR ("|"),
640 AND ("&") and NOT ("!").
641

642

Table 2

Input nodes	Value	Logical diffusion rule	Interpretation
Admp1_In	1	{Admp1[0:],min = 1}	Admp1 takes level 1 if a least one cell expresses Admp1 with no distance restriction
Bmp2_4_In	1	{Bmp2_4[0:], min = 1} & !{Bmp2_4:2[0], min = 1}	Bmp2_4 takes level 1 if at least one cell expresses Bmp2_4 with no distance restriction and the cell does not already express Bmp2_4 at level 2
Bmp2_4_In	2	{Bmp2_4:2[0], min = 1}	Bmp2_4 takes level 2 if the cell already expresses Bmp2_4 at level 2
Chordin_In	1	{Chordin[0:2], min = 1}	Chordin takes level 1 if at least one cell expresses Chordin among the cell itself and its neighbors at a distance equal or lower than two cells
Chordin_In	2	No function	Chordin cannot take level 2 by diffusion
Lefty_In	1	{Nodal:2[0:1], min = 1, max = 2}	Lefty takes level 1 if one or two cell(s) express Nodal at level 2 among the cell itself and its direct neighbors
Nodal_In	2	{Nodal:2[0:1], min = 3}	Nodal takes level 2 if at least three cells express Nodal et level 2 among the cell itself and its direct neighbors
Nodal_In	3	No function	Nodal cannot take level 3 by diffusion
Admp2_In	1	{Admp2[:0],min = 1}	Admp2 takes level 1 if the cell already expresses Admp2
Tolloid_In	*	No function	No Tolloid diffusion
Panda_In	*	No function	No Panda diffusion
Wnt_In	*	No function	No Wnt diffusion

643
644

645 **Table 2. Logical diffusion rules used in Epilog.**

646 Logical rules are used to define the diffusion dynamics perceived by the inputs nodes,
647 depending on the values of the output nodes in the neighbouring cells. Diffusion rules are
648 defined in the format "{N:L[D],S}", with N as the node emitting diffusing signal, L its
649 required activation level, D the distance range to perceive diffusion and S the minimum
650 and/or maximum number of cell required in this state. For example, the seventh row in the
651 table specifies that cells will have their Nodal input node value converging toward the value 2
652 if at least three cells are expressing Nodal at a value 2 at a maximum distance of one cell (i.e.
653 among the target cell itself and its direct neighbours).

654

655 **Figure legends**

656

657 **Figure 1. Panda, Nodal and BMP2/4 signalling directs patterning of the Dorsal/Ventral**
658 **axis of the sea urchin embryo.**

659 Summary of the morphological phenotypes and identity of the ectodermal territories of wild-
660 type (control) embryos and embryos following perturbations of Nodal or BMP signalling.
661 (A) In control embryos, the balance between Nodal and BMP signalling patterns the
662 ectoderm in three main territories: Nodal signalling specifies the ventral ectoderm, BMP2/4
663 signalling specifies the dorsal ectoderm, while a ciliary band develops at the interface
664 between them. (B) The whole ectoderm differentiates into ventral territory when *nodal* is
665 overexpressed. (C) Both Nodal and BMP2/4 signalling are absent in Nodal morphants, which
666 gives rise to an expanded large ciliary band. (D) Following BMP2/4 overexpression, all the
667 ectoderm acquires dorsal identity. (E) In contrast, after BMP2/4 inhibition, ventral territories
668 are not perturbed but an ectopic ciliary band develops in place of the presumptive dorsal
669 ectoderm. (F) Simultaneous perturbation of both the TGF-β related factor Panda and BMP2/4
670 signalling allows the expansion of Nodal signalling to the whole territory resulting in the
671 ventralisation of the ectoderm. The genes, proteins or interactions that are inactive following
672 each perturbation are denoted in light grey. Activation and inhibition interactions are
673 respectively shown by green and red arrows. lv, lateral view. vv, vegetal view.

674

675 **Figure 2. Iterative integration of biological data into the GRN model.**

676 The GRN model has been built through an iterative process. A first version based on
677 literature curation and experimental evidence was set and then simulated in wild-type and
678 perturbation conditions. The results of wild-type and mutant simulations were systematically
679 compared with experimental results. In case of discrepancy, the regulatory graph and the
680 logical rules were refined, and the behaviour of the model was then re-examined through the
681 same process.

682

683 **Figure 3. Logical model integrating the main signalling pathways controlling**
684 **specification the dorsal-ventral axis in the embryo of the sea urchin *Paracentrotus***
685 ***Lividus*.**

686 Relying on a logical formalism, this model was defined and analysed using the software
687 GINsim. Green and red arrows represent activations and repressions, respectively. Ellipsoid
688 and rectangular components represent Boolean and multivalued nodes, respectively. The

689 components in yellow correspond to model inputs. Internal components are coloured
690 according to their domain of expression along the dorsal-ventral axis, i.e. dorsal (green),
691 ventral (blue) or ciliary (pink) regions.
692
693 **Figure 4. BMP2/4 and Nodal signalling antagonize each other to pattern the D/V axis of**
694 **the sea urchin embryo.**
695 (A) Continuous treatments at increasing concentrations with Nodal or BMP2/4 protein from
696 the fertilized egg stage. Treatments with increasing concentrations of BMP2/4 protein
697 progressively dorsalise the embryo at the expense of the ventral territories, as reflected by the
698 expansion of the expression of the dorsal marker *tbx2/3* and the repression of the expression
699 of the ventral marker *chordin*. On the other hand, treatments with increasing concentrations
700 of Nodal protein gradually ventralises the embryo at the expense of the dorsal territories as
701 reflected by the gradual expansion of the expression of the ventral marker *chordin* and the
702 repression of the expression of the dorsal marker *tbx2/3*.
703 (B) Three-hour Nodal or BMP2/4 protein treatments at late blastula and hatching blastula
704 stages are sufficient to cross-antagonise each other signalling pathway. Three-hour Nodal
705 protein treatment at late blastula stage results in rounded-shaped embryos partially
706 ventralised that overexpress the ventral marker *nodal* at the expense of the dorsal marker
707 *tbx2/3*. Complementary, three-hour BMP2/4 protein treatment at hatching or late blastula
708 stages promotes massive pSMAD1/5/8 signalling and results in partially dorsalised embryos
709 that overexpress the dorsal marker *tbx2/3* at the expense of the ventral marker *nodal*. EB,
710 Early Blastula; HB, Hatching Blastula; SB, Swimming Blastula; LB, Late Blastula; MB,
711 Mesenchyme Blastula; V, Ventral; D, Dorsal.
712
713 **Figure 5. Simulation of early 32-cell stage and specification of later stage inputs**
714 By restricting the active input nodes to combinations of Nodal and Panda (A), our unicellular
715 model recapitulates the patterns observed in the 32-cell stage embryos (B upper part, C). In
716 wild-type condition, *panda* is expressed in the presumptive dorsal region and restricts *nodal*
717 expression to the presumptive ventral region (Haillot et al., 2015). The stable states resulting
718 from our ventral wild-type simulation (B upper part) were then used to define the input node
719 values for the simulation of later developmental stages, taking into account the diffusion and
720 shuttling events known to occur from the ventral region to further dorsal territories in this
721 developmental time window (B lower part).
722

723 **Figure 6. Comparison of blastula model simulations and experimental results.**
724 With proper logical rules (see Table 1), inputs and initial state conditions (A), our model
725 gives rise to different stable patterns (B), which qualitatively match experimental results (C-
726 D). Note that, in the simulation of the *chordin* morpholino injection, the model predicts two
727 possible stable patterns in the ventral region, whereas experiments point to a mild ventral
728 territory present in these embryos. In the middle area (C), the organisation of dorsal (green),
729 ventral (blue) and ciliary (pink) territories are schematized based on images of wild-type and
730 morphant embryos (D).
731
732 **Figure 7. Probabilistic time-course simulations of the unicellular model starting with the**
733 **ventral initial state.**
734 Temporal evolutions of the mean activation levels of Goosecoid, Iroquois and Onecut,
735 representing ventral (blue), dorsal (green) and ciliary (pink) phenotypes, respectively. All
736 simulations start from a ventral initial state (orange). The first plot (A) corresponds to the
737 wild type, while the three other ones (B, C, D) correspond to *chordin* knock down conditions.
738 Simulations (A, B) were performed with equal up and down state transition rates. Further
739 simulations were performed using rates favouring the dorsal cascade (C), or favouring the
740 ventral cascade (D) (see supplementary materials and methods for details).
741
742 **Figure 8. Multicellular logical simulations for wild-type and mutant conditions, using**
743 **the software Epilog.**
744 Across the multicellular epithelium, specific logical rules have been defined to model the
745 diffusion of signalling components (A) (see Table 2 for diffusion rules). At the initial state,
746 only Nodal is activated in the presumptive ventral territory (B). Multicellular simulation
747 results for the wild-type and morphant conditions (C) qualitatively match our experimental
748 results. Considering a larger epithelium, we further simulated the injection of *nodal* mRNA in
749 two opposite blastomeres of a four-cell embryo (D), which resulted in an embryo displaying a
750 mirror symmetric pattern of ventral, ciliary and dorsal territories along the dorsal-ventral axis,
751 as observed by (Lapraz et al., 2015).
752
753
754
755

756 **Supplementary figure legends**

757

758 **Supplementary Figure S1. EpiLog simulation of the Lefty morpholino condition.**

759 Starting from the initial state with the Nodal pathway initiated in the ventral region, the
760 Epilog simulation of the *lefty* morpholino condition ultimately results in a fully ventralized
761 stable state. The activity dynamics of the three markers genes *goosecoid* (blue, ventral),
762 *onecut* (pink, ciliary) and *irxa* (green, dorsal) denotes the progressive shift of the ciliary
763 boundary toward the dorsal side, as the loss of Lefty enables Nodal to diffuse freely outside
764 of the ventral region.

765

766 **Supplementary Figure S2. Simulation of the boundary ectoderm in the unicellular**
767 **model.**

768 Stable state obtained with the unicellular model when considering Admp2 and Wnt inputs
769 active. Active nodes (yellow for inputs and green for dorsal nodes) and edges (green for
770 activation and red for inhibition) are shown in colour, inactive ones are shown in grey. This
771 stable state corresponds exactly to the dorsal stable state shown in Figure 6.

772

773 **Supplementary Figure S3. Simulation of *panda* perturbations at the 32-cell stage.**

774 Starting with a restricted combination of inputs with Nodal and Panda, we simulated the 32-
775 cell stage D/V patterning using the unicellular model. In wild-type condition, model
776 predictions (A) correctly recapitulates experimental observations (B). It is also the case for
777 the simulation of Panda loss-of-function, mirroring the fully ventralised phenotype observed
778 upon *panda* Mo injection. Simulations of *panda* overexpression fully abrogate ventral
779 specification and result in a global ciliary band phenotype (A), whereas experimental
780 evidences show no impact of global overexpression of *panda* on the onset of D/V patterning
781 (Haillot et al., 2015) (B).

782

Acknowledgements

We thank Aline Chessel for excellent technical help. We are indebted to Guillaume Lavisse for insightful comments. We thank Aurélie Martres for taking care of the sea urchins. We thank Aurelien Naldi for continuous help and support on the development of the Colomoto Jupyter Notebook. We thank Claudine Chaouiya and Pedro Monteiro for their support regarding the use of EpiLog. We thank Mathurin Dorel for his help in defining a preliminary version of the cellular model.

Funding

This work was supported by a grant from the CNRS, the UNSA, the French Foundation for Cancer Research (ARC) SFI20121205586, and the National Agency for Research (ANR) (grant Echinodal ANR-14-CE11-0006-01 to TL) and the FRM Team project DEQ20180339195 to TL. S. F. has been supported by a grant from the PhD School *Life Science Complexity* (ED 515) and another grant from the *Fondation pour la Recherche Médicale* FDT201904008366. M.D. Molina was supported by an EMBO long-term fellowship and by an ARC postdoctoral fellowship. E. Haillot was supported by a 4th year doctoral fellowship from the ARC. M.T.C. has been further supported by the *Institut Universitaire de France.*

Competing interests

No competing interests declared.

References

Angerer, L. M., Yaguchi, S., Angerer, R. C. and Burke, R. D. (2011). The evolution of nervous system patterning: insights from sea urchin development. *Development* **138**, 3613–3623.

Armstrong, N. and McClay, D. R. (1994). Skeletal pattern is specified autonomously by the primary mesenchyme cells in sea urchin embryos. *Dev. Biol.* **162**, 329–338.

Armstrong, N., Hardin, J. and McClay, D. R. (1993). Cell-cell interactions regulate skeleton formation in the sea urchin embryo. *Dev. Camb. Engl.* **119**, 833–840.

Arnone, M. I. and Davidson, E. H. (1997). The hardwiring of development: organization and function of genomic regulatory systems. *Development* **124**, 1851–1864.

Ben-Zvi, D., Shilo, B.-Z., Fainsod, A. and Barkai, N. (2008). Scaling of the BMP activation gradient in Xenopus embryos. *Nature* **453**, 1205–1211.

Chaouiya, C., Naldi, A. and Thieffry, D. (2012). Logical modelling of gene regulatory networks with GINsim. *Methods Mol. Biol. Clifton NJ* **804**, 463–479.

Chen, D., Zhao, M. and Mundy, G. R. (2004). Bone Morphogenetic Proteins. *Growth Factors* **22**, 233–241.

Cheng, S. K., Olale, F., Brivanlou, A. H. and Schier, A. F. (2004). Lefty Blocks a Subset of TGFβ Signals by Antagonizing EGF-CFC Coreceptors. *PLOS Biol.* **2**, e30.

De Robertis, E. M. (2009). Spemann's organizer and the self-regulation of embryonic fields. *Mech. Dev.* **126**, 925–941.

Duboc, V., Röttinger, E., Besnardeau, L. and Lepage, T. (2004). Nodal and BMP2/4 signaling organizes the oral-aboral axis of the sea urchin embryo. *Dev. Cell* **6**, 397–410.

Duboc, V., Lapraz, F., Besnardeau, L. and Lepage, T. (2008). Lefty acts as an essential modulator of Nodal activity during sea urchin oral-aboral axis formation. *Dev. Biol.* **320**, 49–59.

Duloquin, L., Lhomond, G. and Gache, C. (2007). Localized VEGF signaling from ectoderm to mesenchyme cells controls morphogenesis of the sea urchin embryo skeleton. *Dev. Camb. Engl.* **134**, 2293–2302.

Haillot, E., Molina, M. D., Lapraz, F. and Lepage, T. (2015). The Maternal Maverick/GDF15-like TGF-β Ligand Panda Directs Dorsal-Ventral Axis Formation by Restricting Nodal Expression in the Sea Urchin Embryo. *PLoS Biol.* **13**, 1–38.

Hardin, J., Coffman, J. A., Black, S. D. and McClay, D. R. (1992). Commitment along the dorsoventral axis of the sea urchin embryo is altered in response to NiCl2. *Dev. Camb. Engl.* **116**, 671–685.

Harland, R. M. (1991). In situ hybridization: an improved whole-mount method for Xenopus embryos. *Methods Cell Biol.* **36**, 685–695.

Joubin, K. and Stern, C. D. (2001). Formation and maintenance of the organizer among the vertebrates. *Int. J. Dev. Biol.* **45**, 165–175.

Juan, H. and Hamada, H. (2001). Roles of nodal-lefty regulatory loops in embryonic patterning of vertebrates. *Genes Cells Devoted Mol. Cell. Mech.* **6**, 923–930.

Kimelman, D. and Pyati, U. J. (2005). Bmp signaling: turning a half into a whole. *Cell* **123**, 982–984.

Lapraz, F., Röttinger, E., Duboc, V., Range, R., Duloquin, L., Walton, K., Wu, S.-Y., Bradham, C., Loza, M. A., Hibino, T., et al. (2006). RTK and TGF-beta signaling pathways genes in the sea urchin genome. *Dev. Biol.* **300**, 132–152.

Lapraz, F., Besnardeau, L. and Lepage, T. (2009). Patterning of the dorsal-ventral axis in echinoderms: Insights into the evolution of the BMP-chordin signaling network. *PLoS Biol.* **7**,.

Lapraz, F., Haillot, E. and Lepage, T. (2015). A deuterostome origin of the Spemann organiser suggested by Nodal and ADMPs functions in Echinoderms. *Nat. Commun.* **6**, 8434.

Lele, Z., Nowak, M. and Hammerschmidt, M. (2001). Zebrafish admp is required to restrict the size of the organizer and to promote posterior and ventral development. *Dev. Dyn.* **222**, 681–687.

Lepage, T. and Gache, C. (1989). Purification and characterization of the sea urchin embryo hatching enzyme. *J. Biol. Chem.* **264**, 4787–4793.

Lepage, T. and Gache, C. (1990). Early expression of a collagenase-like hatching enzyme gene in the sea urchin embryo. *EMBO J.* **9**, 3003–3012.

Levine, M. and Davidson, E. H. (2005). Gene regulatory networks for development. *Proc. Natl. Acad. Sci.* **102**, 4936–4942.

Li, E., Materna, S. C. and Davidson, E. H. (2012). Direct and indirect control of oral ectoderm regulatory gene expression by Nodal signaling in the sea urchin embryo. *Dev. Biol.* **369**, 377–385.

Li, E., Materna, S. C. and Davidson, E. H. (2013). New regulatory circuit controlling spatial and temporal gene expression in the sea urchin embryo oral ectoderm GRN. *Dev. Biol.* **382**, 268–279.

Li, E., Cui, M., Peter, I. S. and Davidson, E. H. (2014). Encoding regulatory state boundaries in the pregastrular oral ectoderm of the sea urchin embryo. *Proc. Natl. Acad. Sci.* **111**, E906–E913.

Mbodj, A., Gustafson, E. H., Ciglar, L., Junion, G., Gonzalez, A., Girardot, C., Perrin, L., Furlong, E. E. M. and Thieffry, D. (2016). Qualitative Dynamical Modelling Can Formally Explain Mesoderm Specification and Predict Novel Developmental Phenotypes. *PLoS Comput. Biol.* **12**, 1–17.

McIntyre, D. C., Seay, N. W., Croce, J. C. and McClay, D. R. (2013). Short-range Wnt5 signaling initiates specification of sea urchin posterior ectoderm. *Dev. Camb. Engl.* **140**, 4881–4889.

Molina, M. D., Quirin, M., Haillot, E., De Crozé, N., Range, R., Rouel, M., Jimenez, F., Amrouche, R., Chessel, A. and Lepage, T. (2018). MAPK and GSK3/ß-TRCP-mediated degradation of the maternal Ets domain transcriptional repressor Yan/Tel controls the spatial expression of nodal in the sea urchin embryo. *PLoS Genet.* **14**, e1007621.

Naldi, A. (2018). BioLQM: A Java Toolkit for the Manipulation and Conversion of Logical Qualitative Models of Biological Networks. *Front. Physiol.* **9**, 1605.

Naldi, A., Thieffry, D. and Chaouiya, C. (2007). Decision Diagrams for the Representation and Analysis of Logical Models of Genetic Networks. In *Computational Methods in Systems Biology* (ed. Calder, M.) and Gilmore, S.), pp. 233–247. Berlin, Heidelberg: Springer.

Naldi, A., Hernandez, C., Levy, N., Stoll, G., Monteiro, P. T., Chaouiya, C., Helikar, T., Zinovyev, A., Calzone, L., Cohen-Boulakia, S., et al. (2018). The CoLoMoTo Interactive Notebook: Accessible and Reproducible Computational Analyses for Qualitative Biological Networks. *Front. Physiol.* **9**,.

Peter, I. S. (2019). Chapter 2 - Methods for the experimental and computational analysis of gene regulatory networks in sea urchins. In *Methods in Cell Biology* (ed. Hamdoun, A.) and Foltz, K. R.), pp. 89–113. Academic Press.

Peter, I. S., Faure, E. and Davidson, E. H. (2012). Predictive computation of genomic logic processing functions in embryonic development. *Proc. Natl. Acad. Sci.* **109**, 16434–16442.

Range, R., Lapraz, F., Quirin, M., Marro, S., Besnardeau, L. and Lepage, T. (2007). Cis-regulatory analysis of nodal and maternal control of dorsal-ventral axis formation by Univin, a TGF-β related to Vg1. *Development* **134**, 3649–3664.

Reversade, B. and De Robertis, E. M. (2005). Regulation of ADMP and BMP2/4/7 at opposite embryonic poles generates a self-regulating morphogenetic field. *Cell* **123**, 1147–1160.

Röttinger, E., Saudemont, A., Duboc, V., Besnardeau, L., McClay, D. and Lepage, T. (2008). FGF signals guide migration of mesenchymal cells, control skeletal morphogenesis [corrected] and regulate gastrulation during sea urchin development. *Dev. Camb. Engl.* **135**, 353–365.

Sakuma, R., Ohnishi, Y., Meno, C., Fujii, H., Juan, H., Takeuchi, J., Ogura, T., Li, E., Miyazono, K. and Hamada, H. (2002). Inhibition of Nodal signalling by Lefty mediated through interaction with common receptors and efficient diffusion. *Genes Cells* **7**, 401–412.

Saudemont, A., Haillot, E., Mekpoh, F., Bessodes, N., Quirin, M., Lapraz, F., Duboc, V., Röttinger, E., Range, R., Oisel, A., et al. (2010). Ancestral Regulatory Circuits Governing Ectoderm Patterning Downstream of Nodal and BMP2/4 Revealed by Gene Regulatory Network Analysis in an Echinoderm. *PLOS Genet.* **6**, e1001259.

Stoll, G., Caron, B., Viara, E., Dugourd, A., Zinovyev, A., Naldi, A., Kroemer, G., Barillot, E. and Calzone, L. (2017). MaBoSS 2.0: an environment for stochastic Boolean modeling. *Bioinformatics* **33**, 2226–2228.

Su, Y.-H., Li, E., Geiss, G. K., Longabaugh, W. J. R., Krämer, A. and Davidson, E. H. (2009). A perturbation model of the gene regulatory network for oral and aboral ectoderm specification in the sea urchin embryo. *Dev. Biol.* **329**, 410–421.

Thomas, R. (1991). Regulatory networks seen as asynchronous automata: A logical description. *J. Theor. Biol.* **153**, 1–23.

Thomas, R. and D'Ari, R. (1990). *Biological feedback*. Boca Raton, FL etc.: CRC Press.

Varela, P. L., Ramos, C. V., Monteiro, P. T. and Chaouiya, C. (2019). EpiLog: A software for the logical modelling of epithelial dynamics. *F1000Research* **7**, 1145.

Wilczynski, B. and Furlong, E. E. M. (2010). Challenges for modeling global gene regulatory networks during development: Insights from Drosophila. *Dev. Biol.* **340**, 161–169.

Willot, V., Mathieu, J., Lu, Y., Schmid, B., Sidi, S., Yan, Y.-L., Postlethwait, J. H., Mullins, M., Rosa, F. and Peyriéras, N. (2002). Cooperative Action of ADMP- and BMP-Mediated Pathways in Regulating Cell Fates in the Zebrafish Gastrula. *Dev. Biol.* **241**, 59–78.

Figure 1

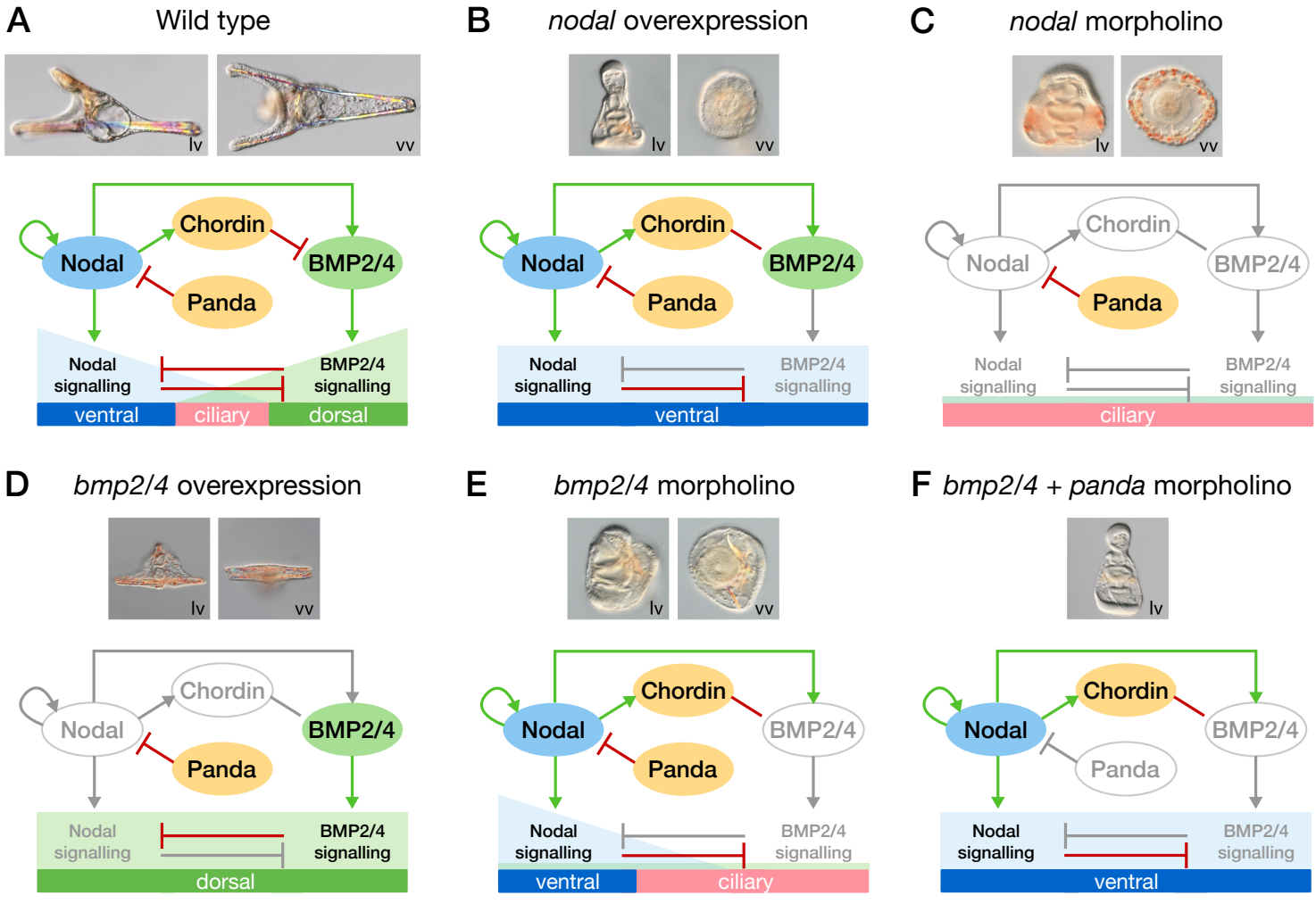
A
Wild type
lv
vv
Nodal
Chordin
BMP2/4
Panda
Nodal signalling
BMP2/4 signalling
ventral
ciliary
dorsal
B
nodal overexpression
lv
vv
Nodal
Chordin
BMP2/4
Panda
Nodal signalling
BMP2/4 signalling
ventral
C
nodal morpholino
lv
vv
Nodal
Chordin
BMP2/4
Panda
Nodal signalling
BMP2/4 signalling
ciliary
D
bmp2/4 overexpression
lv
vv
Nodal
Chordin
BMP2/4
Panda
Nodal signalling
BMP2/4 signalling
dorsal
E
bmp2/4 morpholino
lv
vv
Nodal
Chordin
BMP2/4
Panda
Nodal signalling
BMP2/4 signalling
ventral
ciliary
F
bmp2/4 + panda morpholino
lv
Nodal
Chordin
BMP2/4
Panda
Nodal signalling
BMP2/4 signalling
ventral

Figure 2

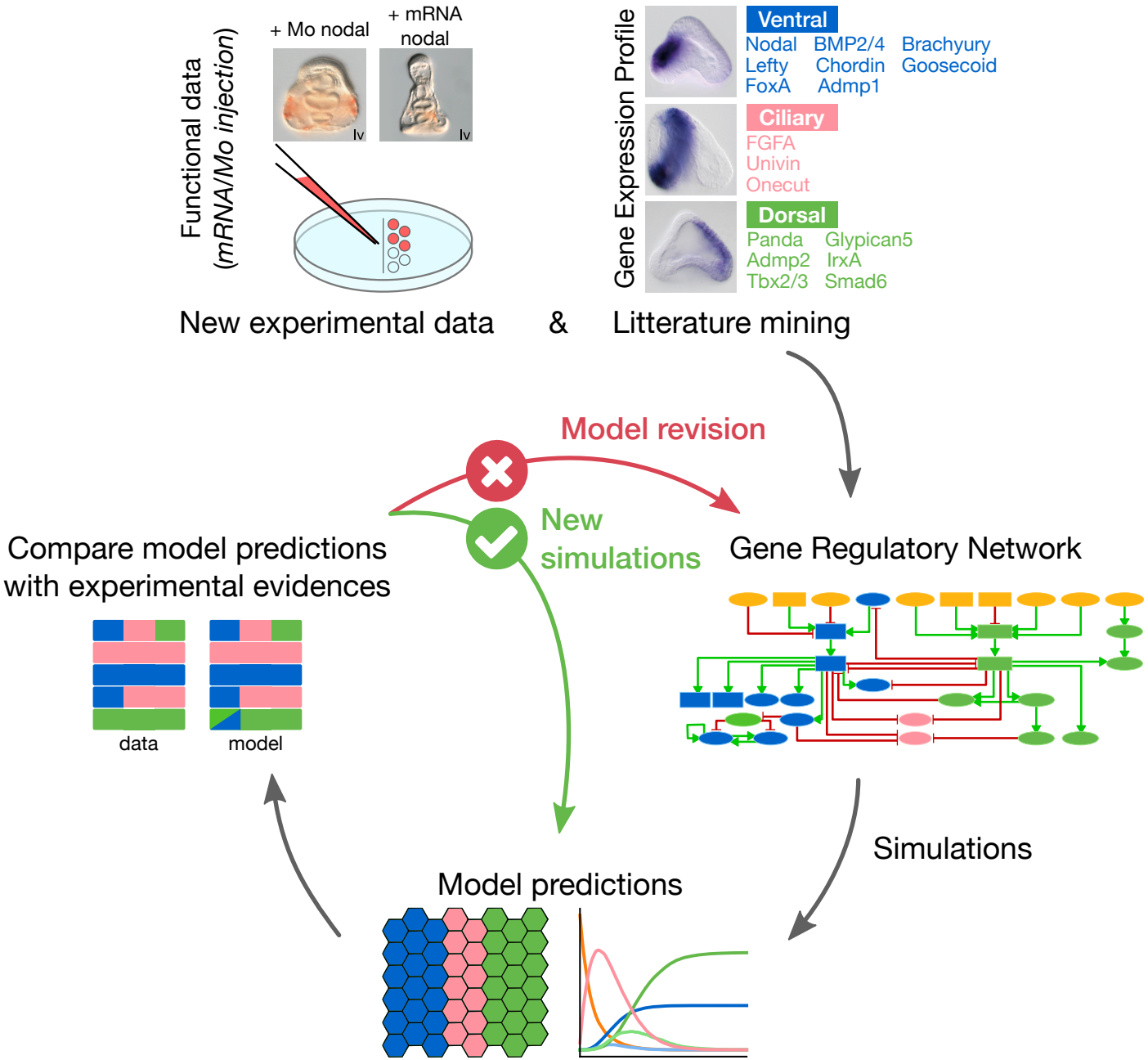
Functional data
(mRNA/Mo injection)
+ Mo nodal
+ mRNA nodal
lv
lv
Gene Expression Profile
Ventral
Nodal
BMP2/4
Brachyury
Lefty
Chordin
Goosecoid
FoxA
Admp1
Ciliary
FGFA
Univin
Onecut
Dorsal
Panda
Glypican5
Admp2
IrxA
Tbx2/3
Smad6
New experimental data
&
Litterature mining
Model revision
New simulations
Compare model predictions with experimental evidences
data
model
Gene Regulatory Network
Simulations
Model predictions

Figure 3

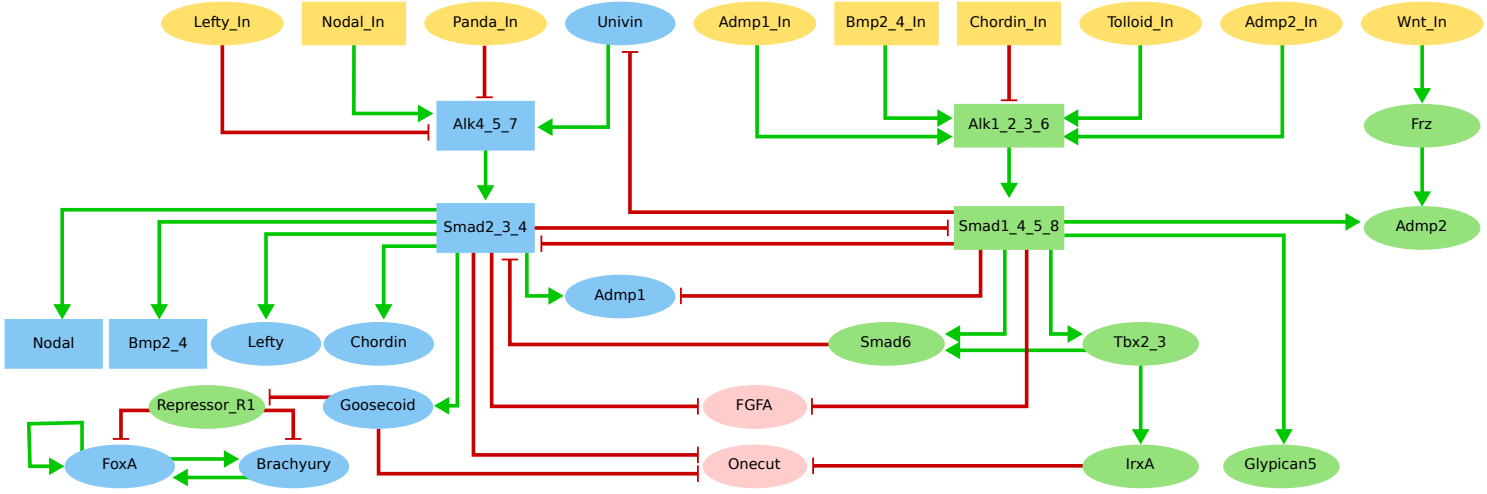
Lefty_In
Nodal_In
Panda_In
Univin
Admp1_In
Bmp2_4_In
Chordin_In
Tolloid_In
Admp2_In
Wnt_In
Alk4_5_7
Alk1_2_3_6
Frz
Smad2_3_4
Smad1_4_5_8
Admp2
Admp1
Nodal
Bmp2_4
Lefty
Chordin
Smad6
Tbx2_3
Repressor_R1
Goosecoid
FGFA
FoxA
Brachyury
Onecut
IrxA
Glypican5

Figure 4

A

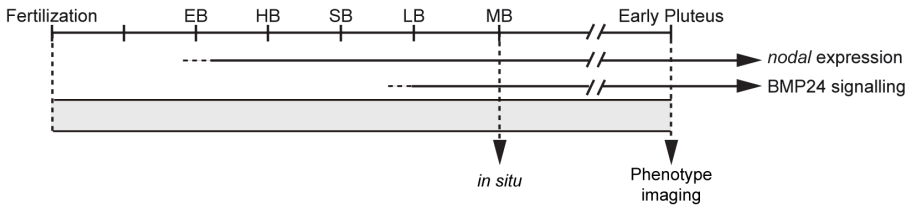
Fertilization
EB
HB
SB
LB
MB
Early Pluteus
nodal expression
BMP24 signalling
in situ
Phenotype imaging

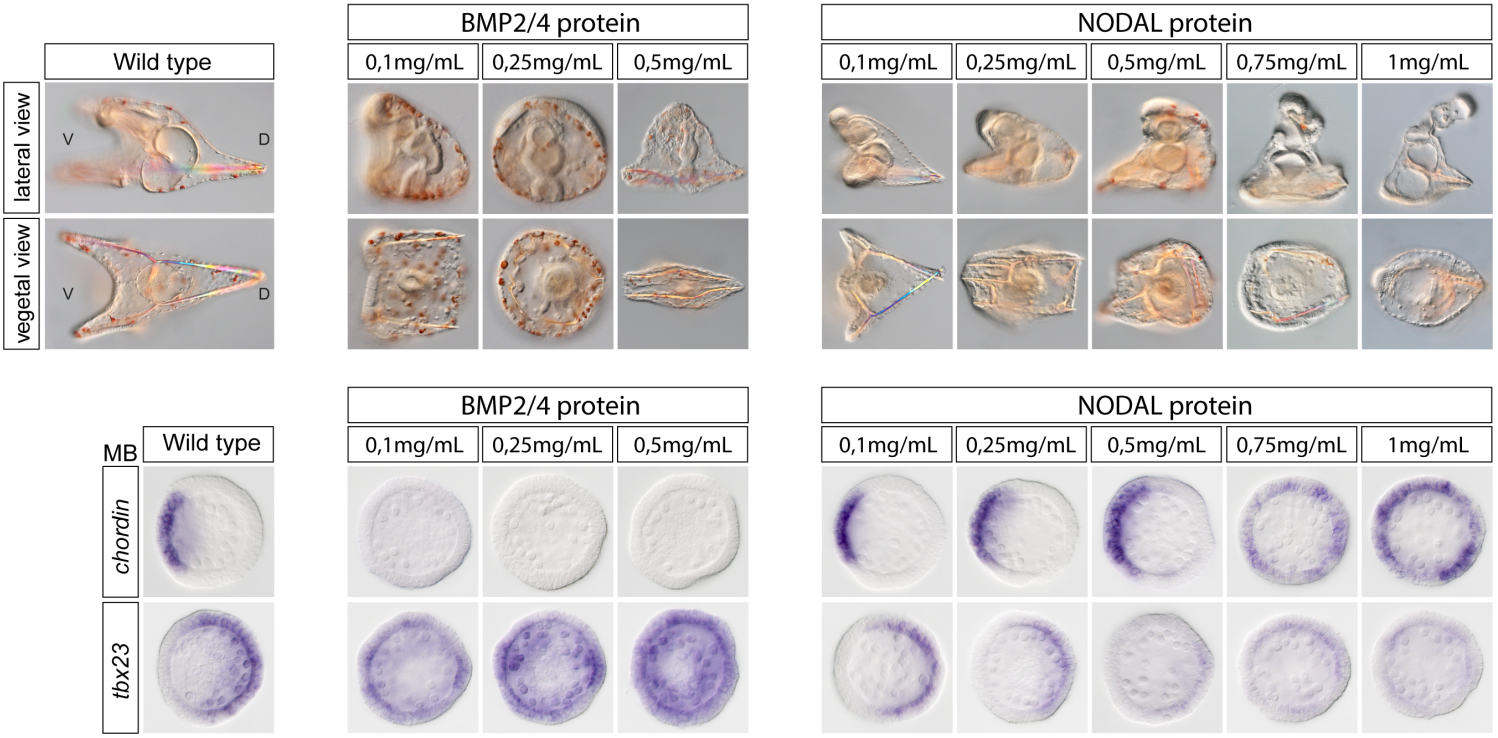
Wild type
BMP2/4 protein
0,1mg/mL
0,25mg/mL
0,5mg/mL
NODAL protein
0,1mg/mL
0,25mg/mL
0,5mg/mL
0,75mg/mL
1mg/mL
lateral view
vegetal view
V
D
MB
chordin
tbx23

B

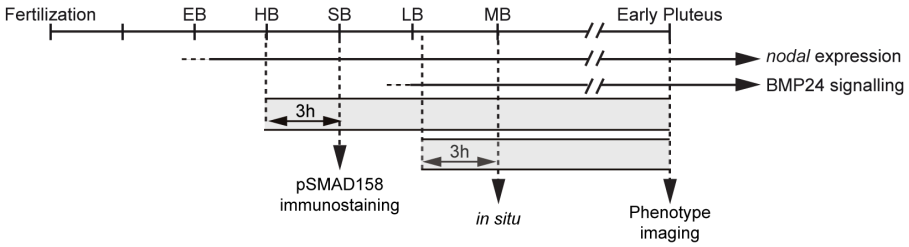
Fertilization
EB
HB
SB
LB
MB
Early Pluteus
nodal expression
BMP24 signalling
3h
3h
pSMAD158 immunostaining
in situ
Phenotype imaging

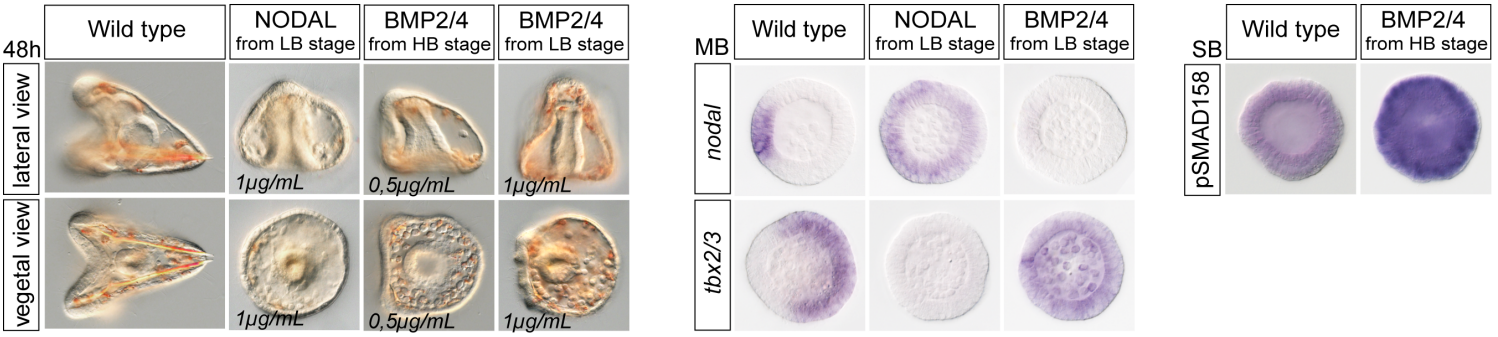
48h
Wild type
NODAL from LB stage
BMP2/4 from HB stage
BMP2/4 from LB stage
lateral view
vegetal view
1µg/mL
0,5µg/mL
1µg/mL
1µg/mL
0,5µg/mL
1µg/mL
MB
nodal
tbx2/3
SB
pSMAD158
BMP2/4 from HB stage

Figure 5

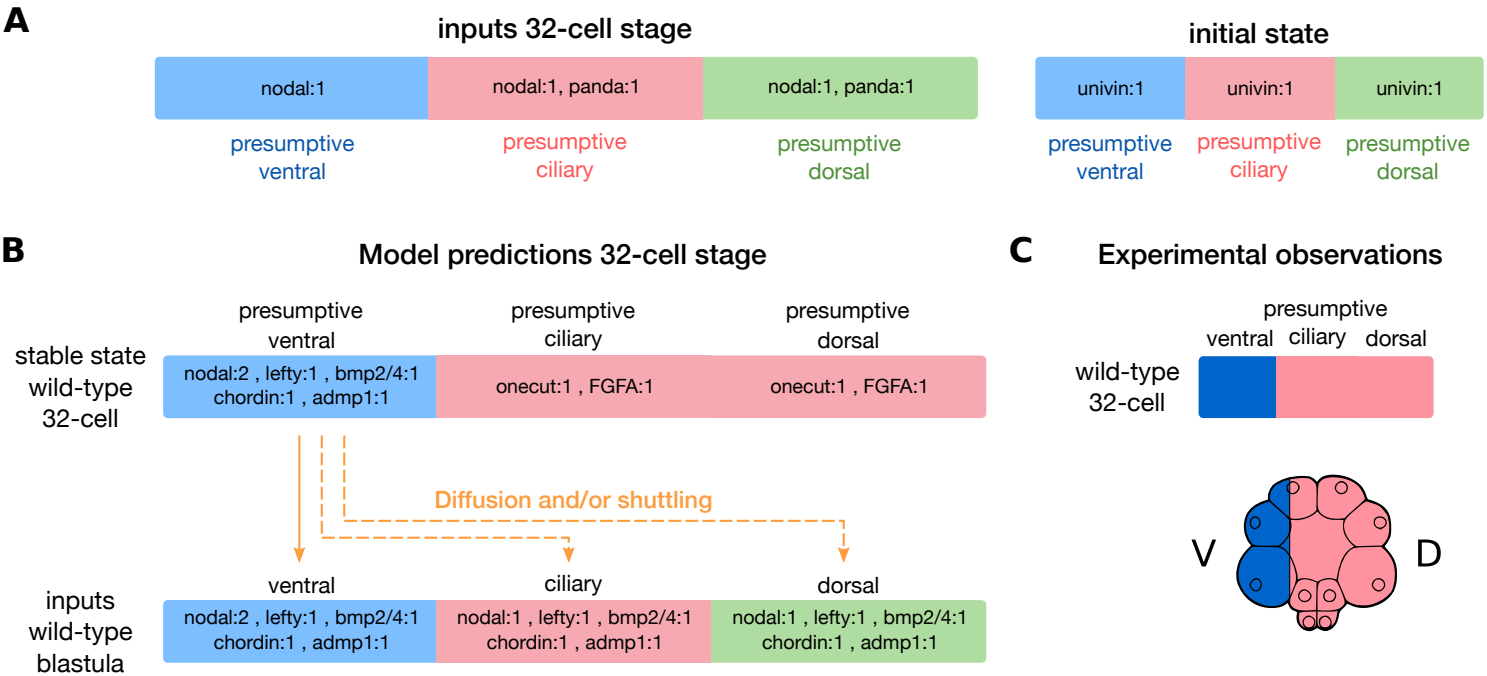
A
inputs 32-cell stage
nodal:1
nodal:1, panda:1
nodal:1, panda:1
presumptive ventral
presumptive ciliary
presumptive dorsal
initial state
univin:1
univin:1
univin:1
presumptive ventral
presumptive ciliary
presumptive dorsal
B
Model predictions 32-cell stage
presumptive ventral
presumptive ciliary
presumptive dorsal
stable state wild-type 32-cell
nodal:2 , lefty:1 , bmp2/4:1 chordin:1 , admp1:1
onecut:1 , FGFA:1
onecut:1 , FGFA:1
Diffusion and/or shuttling
ventral
ciliary
dorsal
inputs wild-type blastula
nodal:2 , lefty:1 , bmp2/4:1 chordin:1 , admp1:1
nodal:1 , lefty:1 , bmp2/4:1 chordin:1 , admp1:1
nodal:1 , lefty:1 , bmp2/4:1 chordin:1 , admp1:1
C
Experimental observations
presumptive
ventral
ciliary
dorsal
wild-type 32-cell
V
D

Figure 6

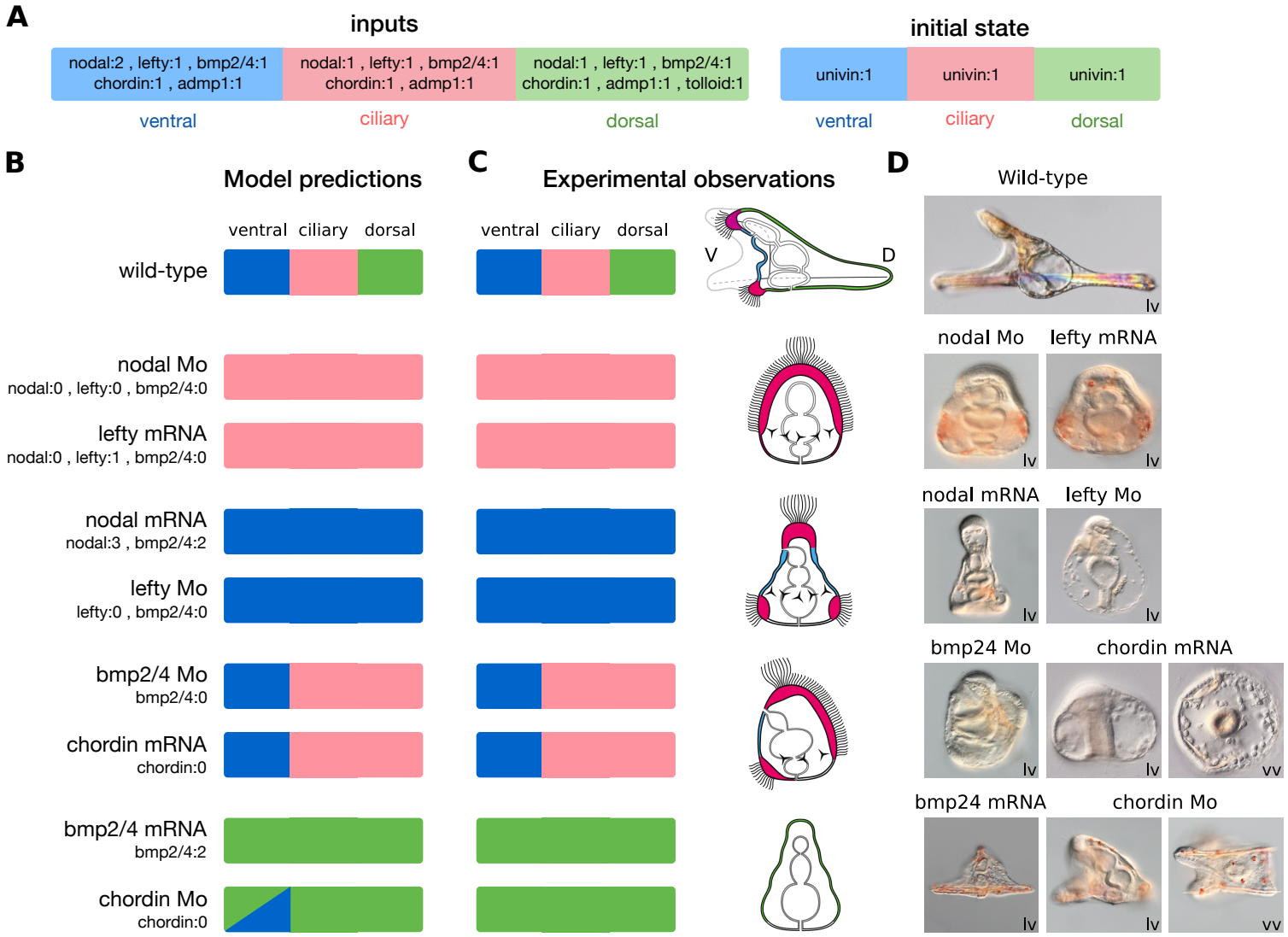
A
inputs
nodal:2 , lefty:1 , bmp2/4:1
chordin:1 , admp1:1
nodal:1 , lefty:1 , bmp2/4:1
chordin:1 , admp1:1
nodal:1 , lefty:1 , bmp2/4:1
chordin:1 , admp1:1 , tolloid:1
ventral
ciliary
dorsal
initial state
univin:1
univin:1
univin:1
ventral
ciliary
dorsal
B
Model predictions
ventral ciliary dorsal
wild-type
nodal Mo
nodal:0 , lefty:0 , bmp2/4:0
lefty mRNA
nodal:0 , lefty:1 , bmp2/4:0
nodal mRNA
nodal:3 , bmp2/4:2
lefty Mo
lefty:0 , bmp2/4:0
bmp2/4 Mo
bmp2/4:0
chordin mRNA
chordin:0
bmp2/4 mRNA
bmp2/4:2
chordin Mo
chordin:0
C
Experimental observations
ventral ciliary dorsal
V
D
D
Wild-type
lv
nodal Mo
lefty mRNA
lv
lv
nodal mRNA
lefty Mo
lv
lv
bmp24 Mo
chordin mRNA
lv
lv
vv
bmp24 mRNA
chordin Mo
lv
lv
vv

Figure 7

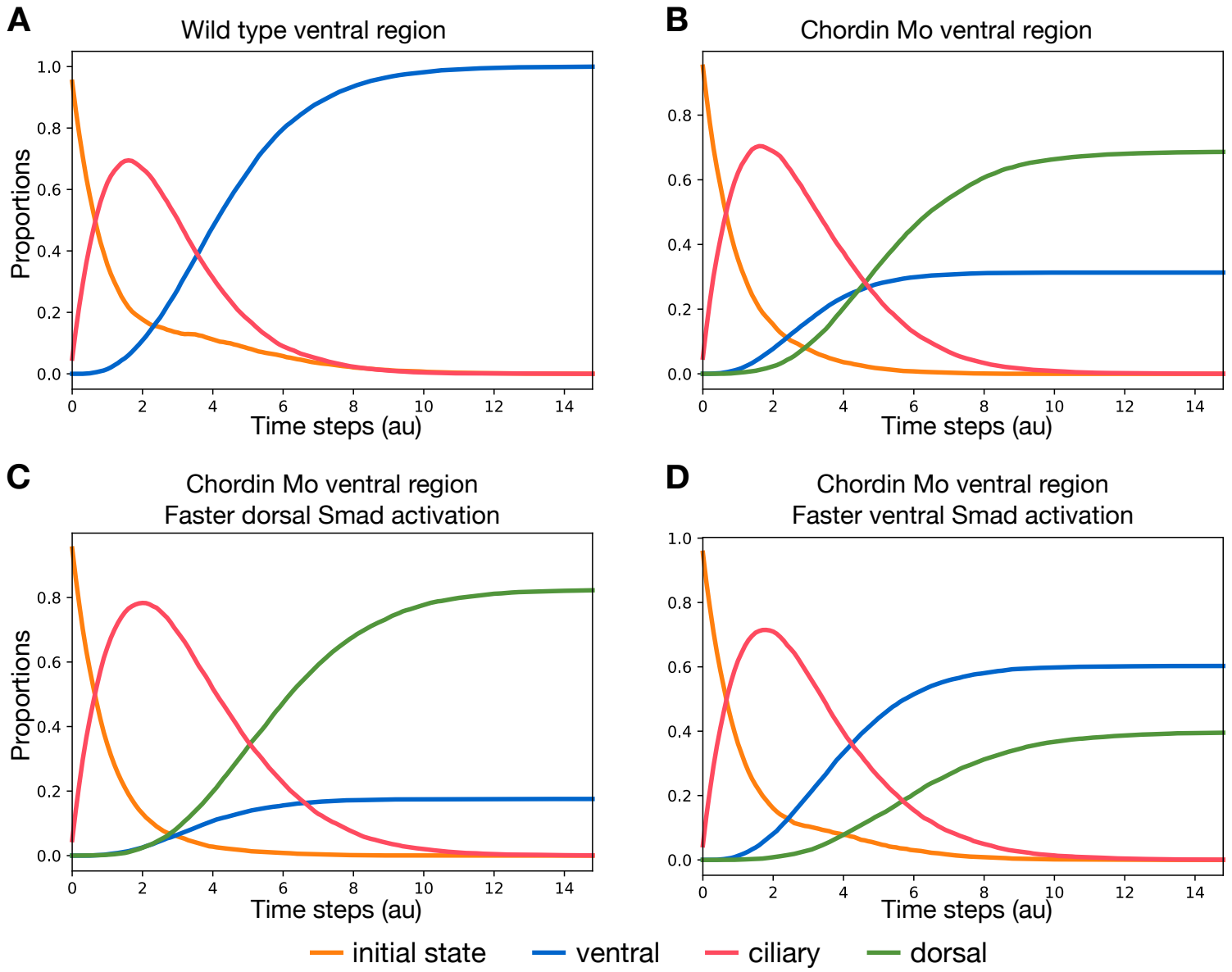
A
Wild type ventral region
Proportions
Time steps (au)
B
Chordin Mo ventral region
Time steps (au)
C
Chordin Mo ventral region
Faster dorsal Smad activation
Proportions
Time steps (au)
D
Chordin Mo ventral region
Faster ventral Smad activation
Time steps (au)
initial state
ventral
ciliary
dorsal

Figure 8

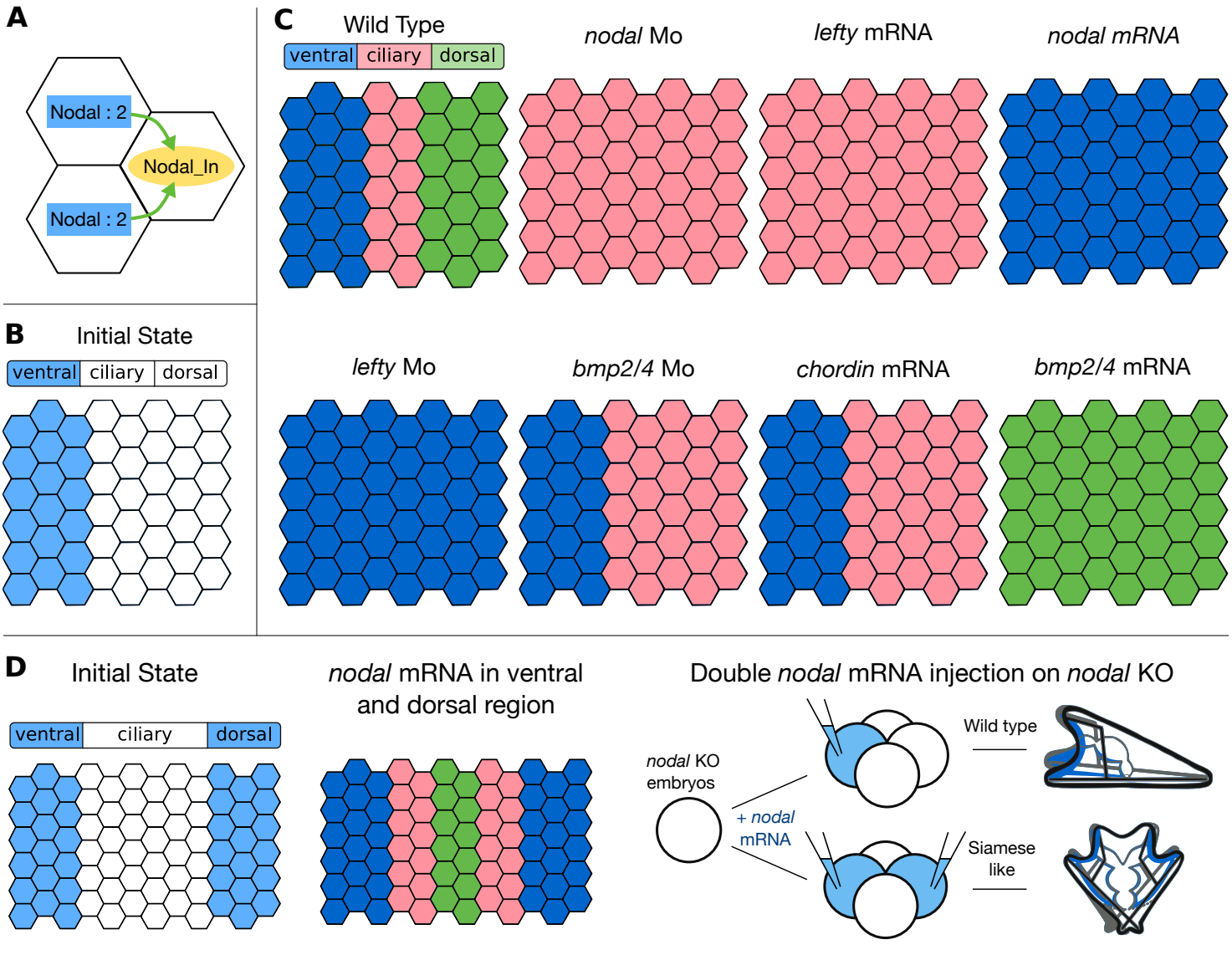
A
Nodal : 2
Nodal_In
Nodal : 2
B
Initial State
ventral
ciliary
dorsal
C
Wild Type
ventral
ciliary
dorsal
nodal Mo
lefty mRNA
nodal mRNA
lefty Mo
bmp2/4 Mo
chordin mRNA
bmp2/4 mRNA
D
Initial State
ventral
ciliary
dorsal
nodal mRNA in ventral and dorsal region
Double nodal mRNA injection on nodal KO
nodal KO embryos
+ nodal mRNA
Wild type
Siamese like

Supplementary Figure 1

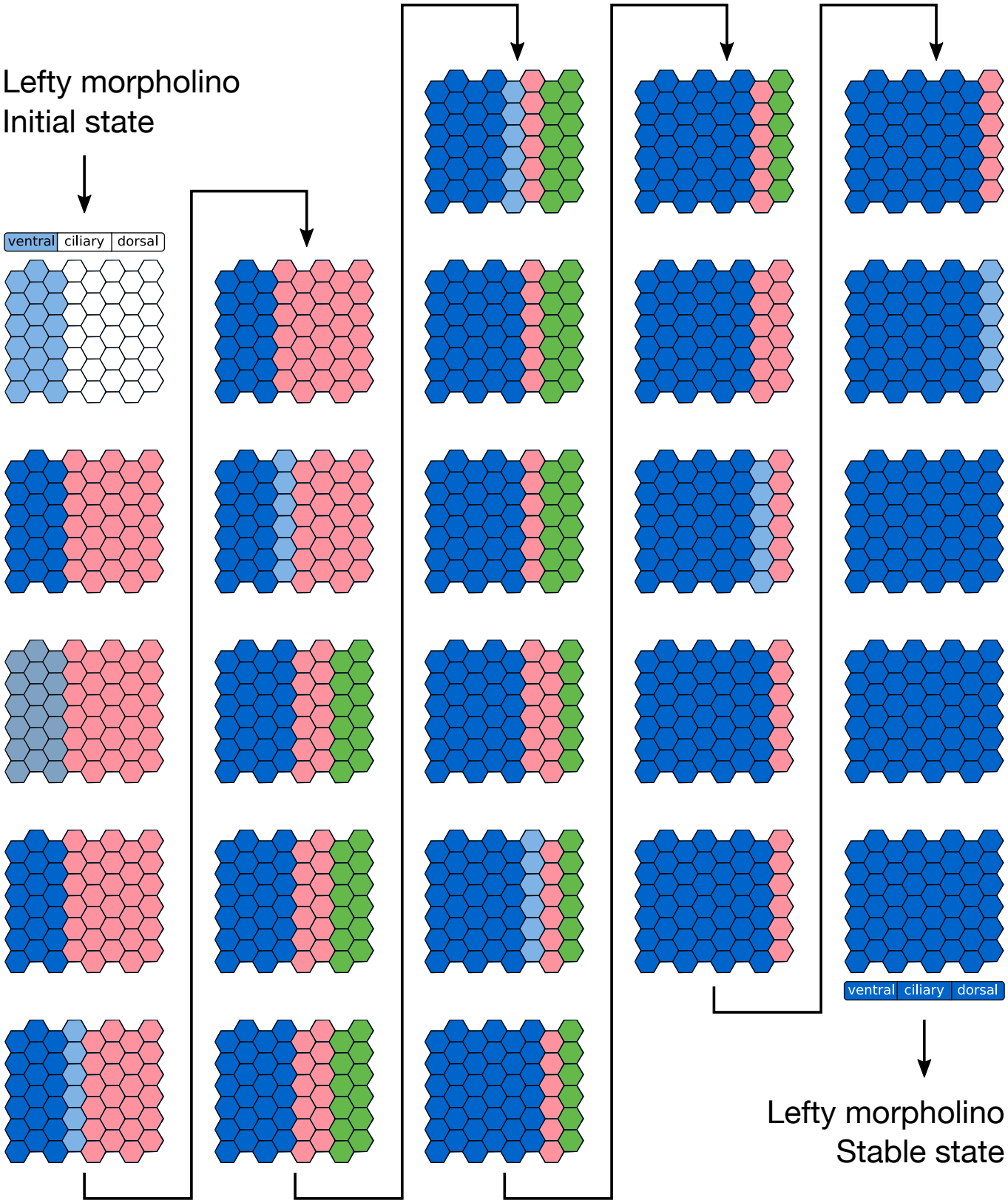

Supplementary Figure 2

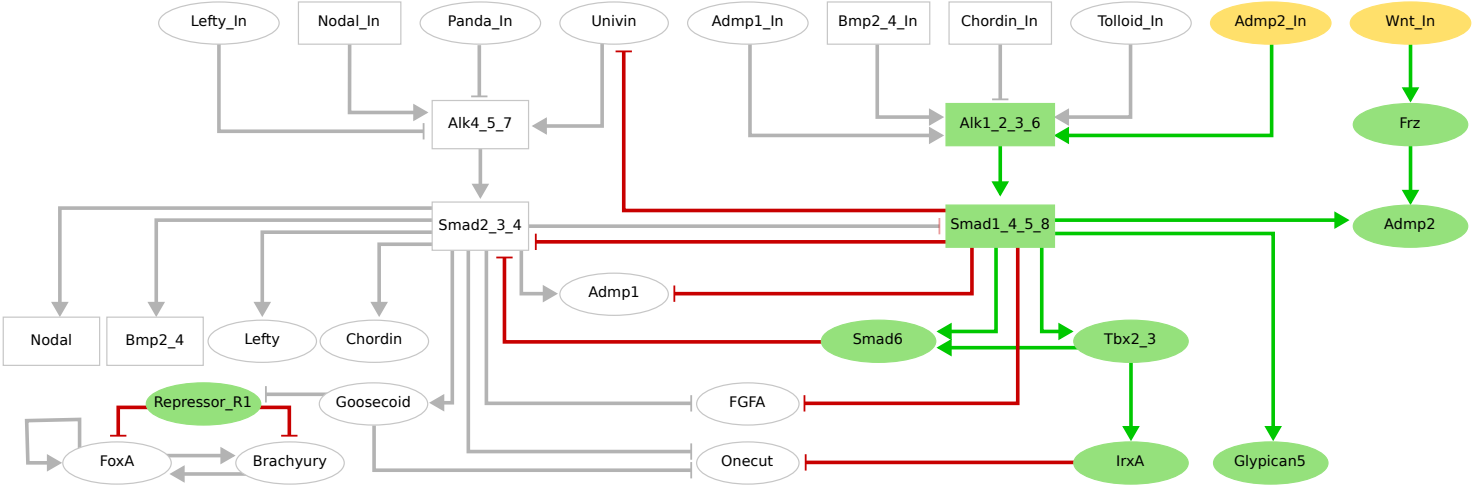
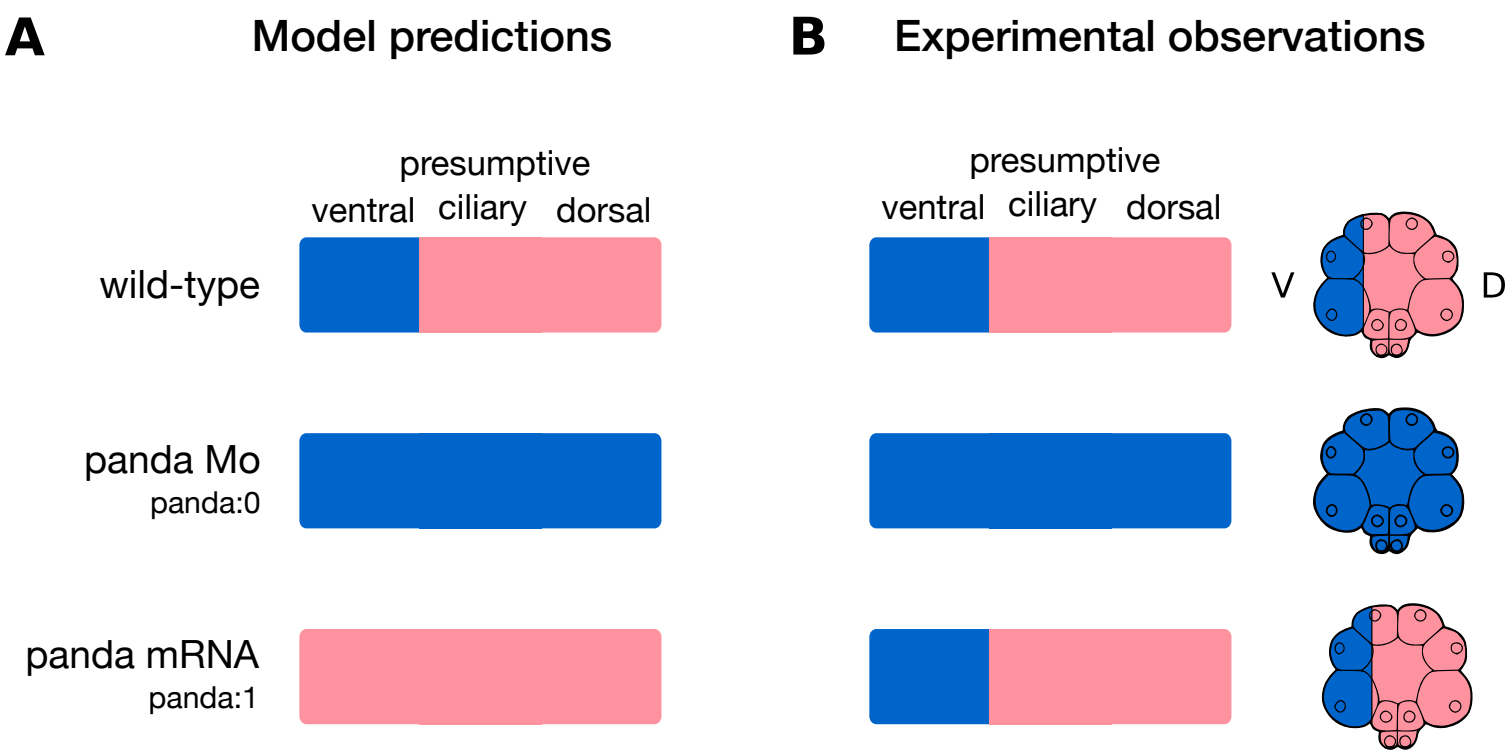
Supplementary Figure 3